

NOAA Technical Report ERL 381-APCL 40



Simulation of Cold Cloud Precipitation in a Three-Dimensional Mesoscale Model

Charles F. Chappell
David R. Smith

October 1976

U. S. DEPARTMENT OF COMMERCE
National Oceanic and Atmospheric Administration
Environmental Research Laboratories





Simulation of Cold Cloud Precipitation in a Three-Dimensional Mesoscale Model

Charles F. Chappell
David R. Smith

Atmospheric Physics and Chemistry Laboratory
Boulder, Colorado

October 1976

U. S. DEPARTMENT OF COMMERCE

Elliot Richardson, Secretary

National Oceanic and Atmospheric Administration
Robert M. White, Administrator

Environmental Research Laboratories
Wilmot Hess, Director





CONTENTS

	Page
Abstract	1
1. INTRODUCTION	1
2. MODEL CHARACTERISTICS	2
3. MODEL EQUATIONS	3
3.1. NUCLEATION	3
3.2 ICE GROWTH AND SUBLIMATION	4
3.2.1. Unrimed Crystals	4
3.2.2. Partially Rimed Crystals	5
3.2.3. Graupel	6
3.3. SEDIMENTATION AND FLUX DIVERGENCE	7
3.3.1. Unrimed Crystals	7
3.3.2. Partially Rimed Crystals	7
3.3.3. Graupel	8
3.4. ELIMINATION OF ICE PARTICLES BY SUBLIMATION	8
3.4.1. Unrimed Crystals	8
3.4.2. Partially Rimed Crystals	9
3.4.3. Graupel	9
3.5. CONVERSION FUNCTIONS	9
3.5.1. Transfer of Unrimed to Partially Rimed Crystals	9
3.5.2. Transfer of Partially Rimed Crystals to Graupel	10
3.6. PREDICTION EQUATIONS	11
3.6.1. Unrimed Crystals	11
3.6.2. Partially Rimed Crystals	11
3.6.3. Graupel	12
4. DYNAMICAL MODEL AND INITIAL CONDITIONS	12
4.1. CHARACTERISTICS OF THE DYNAMICAL MODEL	12
4.2. TOPOGRAPHY	13
4.3. INITIAL CONDITIONS	14
5. NUMERICAL RESULTS	14
6. SUMMARY AND DISCUSSION	23
7. ACKNOWLEDGMENTS	24
8. REFERENCES	24
Appendix: SYMBOLS	25



SIMULATION OF COLD CLOUD PRECIPITATION IN A THREE-DIMENSIONAL MESOSCALE MODEL

Charles F. Chappell
David R. Smith

A cold cloud microphysical model is developed and merged with a 15-level primitive equation mesoscale dynamical model. The microphysical model partitions ice particles into three categories: unrimed, partially rimed, and graupel. Each is considered to have a Marshall-Palmer distribution, and is assigned its own set of physical characteristics. Criteria for converting from one ice particle category to another are based on a comparison of accretional to depositional growth rates. Six prognostic equations predict the concentration and mixing ratio for each ice particle category. Processes in the model include deposition, accretion, condensation, evaporation, sublimation, nucleation, and sedimentation. Microphysical processes are coupled back into the dynamical prediction equations so that the effect of ice processes on the air flow can be investigated. The mesoscale model is used to investigate numerically the development and distribution of snowfall over a mountain massif during a 4500-second integration. It appears to simulate realistically the nucleation and growth of ice particles and their transport and sedimentation to the mountain surface. Snowfall distribution, including the leeward extent of precipitation, also appears reasonable and consistent with that observed along the continental divide of Colorado for similar wind regimes. When further developed the model will be applicable to studies relating to prediction and modification of snowfall over mountainous terrain.

1. INTRODUCTION

Models link theory and observations. During model development current knowledge is evaluated and organized into a coherent entity. This task includes identification of the relevant physics, differentiation of the importance of various physical processes to the specific problem and modeling goal, and formulation of the vital processes into a coherent set of physical concepts defined by mathematical expressions. The accomplishment of this task then allows one to compare theory with observations, and eventually extends those observations both spatially and temporally through prediction.

Application of numerical models to weather modification problems provides a physical

rationale for modification attempts by 1) permitting numerical testing of modification hypotheses prior to field experimentation, 2) better defining the observations required to evaluate hypotheses, and 3) more clearly designating measurements and the instrumentation needed to acquire relevant observations. Numerical models also have application in designing operational programs to produce maximum benefits.

Forecasts of precipitation from cold orographic clouds depend upon satisfactory predictions of airflow over mountainous terrain, and realistic treatment of the interactions of microphysical processes at various levels

within the cloud. Current models that predict mountain snowfall are limited by their one-dimensional or two-dimensional nature, assumptions of cloud homogeneity, or inadequate treatment of settling particles. Examples of these are the models of Jiusto (1971), Cotton (1972), Hobbs et al. (1973), Chappell and Johnson (1974), and Plooster and Fukuta (1975). Young (1974) developed a microphysical model that extended treatment of cloud processes to more than one level through use of a continuous bin technique. Since Young modeled only microphysical processes (prediction equations for air flow were not included), he was able to treat them in considerable detail.

Many important processes related to snowfall over mountainous terrain can be simulated only by three-dimensional models. Blocking, deflection, and funneling of air flow over mountainous terrain are examples. These processes affect cloud formation and the spatial distributions of cloud condensate and precipitation. Thus in order to include such processes, a three-dimensional mesoscale dynamical model has been developed and combined with a cold cloud microphysical model. This paper describes mainly the cold cloud microphysical model, and discusses its application to the prediction of snowfall over complex mountainous terrain. A detailed description of the dynamical model is given by Nickerson and Magaziner (1976).

2. MODEL CHARACTERISTICS

In the development of the microphysical model presented here, the desire for more detail has been tempered by the usual limitations imposed by computer storage and economics. The overall approach has placed equal emphasis on the prediction of dynamical and microphysical processes, which has made it necessary to parameterize certain aspects of the precipitation process. However, this approach has also permitted the coupling of the microphysical thermodynamic forcing to the governing dynamical equations so that the dynamic response of the air flow to condensation and ice growth is quantitatively defined.

In developing this microphysical model, the approach was to treat ice growth and sublimation in greater detail than condensation and evaporation processes. Microphysical processes included in the model are shown in the flow diagram of Figure 1. Liquid cloud water is formed in the model if the saturation vapor mixing ratio is less than the predicted total mixing ratio of water vapor plus liquid cloud water, since supersaturation with respect to water is not allowed. Condensation is the only source of liquid cloud water since melting is not considered. Evaporation of liquid cloud water occurs when the total mixing ratio of water vapor plus liquid cloud water is predicted to be less than

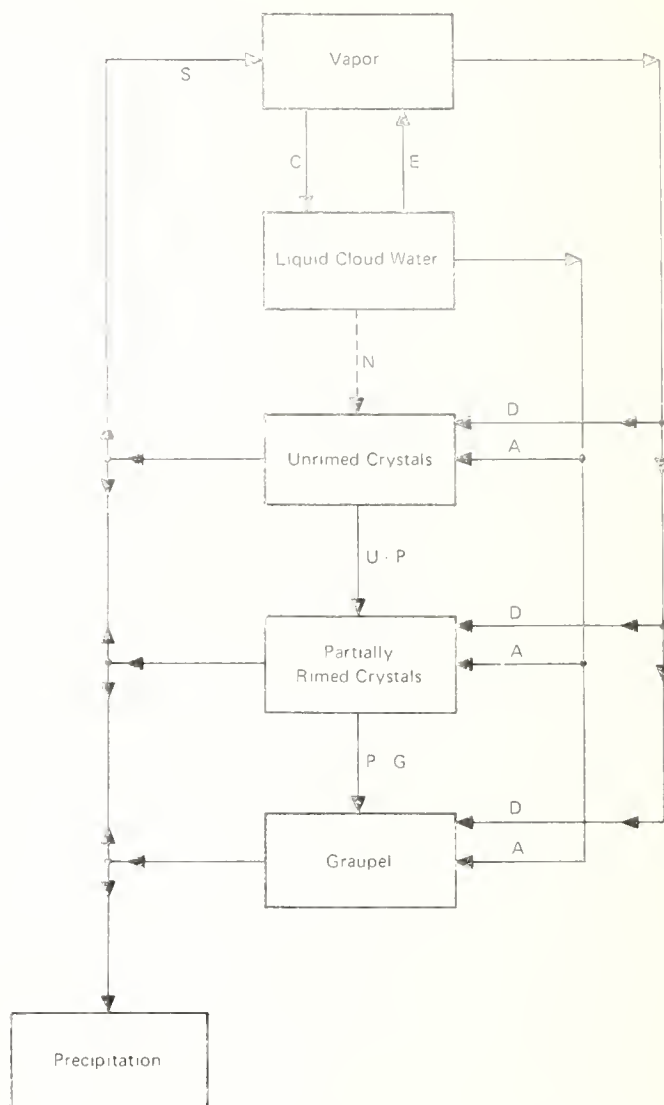


Figure 1. Schematic diagram showing microphysical processes included in the model. Processes are: accretional growth (A), condensation (C), depositional growth (D), evaporation (E), sublimation (S), nucleation (N), conversion of partially rimed crystals to graupel (P-G), and conversion of unrimed crystals to partially rimed crystals (U-P).

the saturation vapor mixing ratio. The moisture source for ice growth can be both vapor and liquid cloud water. Precipitation occurs only as snow and the amount is equal to the ice exiting the liquid water cloud plus any growth, or minus any sublimation, that occurs below water saturation during transit to the surface.

Ice particles are nucleated whenever effective ice nuclei and liquid cloud water are present simultaneously. The rate of nucleation depends on a temperature activation spectrum for ice nuclei and the temperature and cooling rate predicted by the mesoscale dynamical model. At the present time, no attempt is made to include effects of supersaturation on ice nucleation or ice crystal multiplication. Perhaps these features can be added in the future when they are better understood and can be expressed in terms of variables predicted by the model.

The total ice particle population is partitioned into three categories; unrimed crystals, partially rimed crystals and graupel. Conversion from one category to another is dependent on the ratio of crystal growth by accretion to growth by deposition. Prediction equations for the mixing ratio of ice within the three particle categories are formulated within an Eulerian framework. Three additional prediction equations for the corresponding particle concentrations close the system of equations. Particles within the three categories are constrained by integrable size distribution functions that depend upon ice mixing ratio and crystal concentration. Truncated Marshall-Palmer distributions are employed for the three categories. These distribution functions permit the growth equations for individual crystals to be converted into growth equations for individual ice categories. Observations of graupel and planar crystals in Colorado mountain snowfall (Vardiman and Hartzell, 1973) suggest that particles below cloud base have size distributions that might be approximated by an exponential relation (Figs. 2 and 3).

3. MODEL EQUATIONS

Prediction equations for the concentration and mixing ratio of ice in the form of unrimed, partially rimed, and graupel particles can be formulated by considering nucleation, ice growth, sublimation, sedimentation, flux divergence processes, and the rates at which crystals convert from one ice category to another. Expressions for these processes are formulated below for an x , y , z coordinate system using the meter-kilogram-second system of units. A list of symbols is included in the Appendix.

3.1. NUCLEATION

The temperature activation spectra of natural and artificial ice nuclei are often approximated by exponential functions for temperatures above that corresponding to homogeneous nucleation ($< 235\text{K}$), or

$$\frac{\partial N_n}{\partial T} = -aN_n \exp [a(273.16-T)]. \quad (1)$$

Chappell (1970) reported values of 0.2575 m^{-3} and 0.435 K^{-1} for N_n and a , respectively, for an average activation spectrum observed during non-seeded days of the Climax Experiment. These values are used in the integration that is reported on in a later section. The observed flattening of activation spectra at extremely cold temperatures is approximated by assigning a value of 235K to the temperature in (1) for all temperatures below 235K .

Unrimed crystals are nucleated when super-cooled cloud water ($\geq 10^{-5} \text{ kgm kgm}^{-1}$) and cooling exist simultaneously. From (1) the particle nucleation rate is then

$$C_n = \frac{\partial N_n}{\partial T} \frac{dT}{dt}, \quad (2)$$

and the rate at which ice is introduced into a unit mass of air is

$$P_n = \frac{m_n}{\rho} \frac{\partial N_n}{\partial T} \frac{dT}{dt}, \quad (3)$$

where m_n is the average mass of a new crystal just after nucleation. Air density and the cooling rate are output from the mesoscale dynamical model.

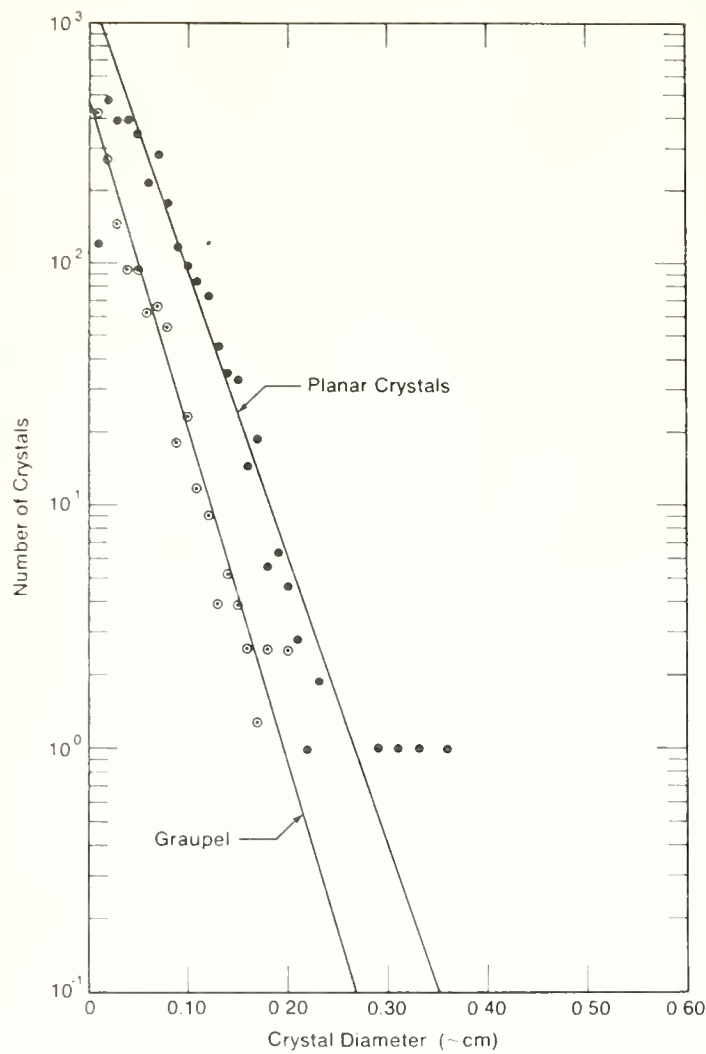


Figure 2. Distribution of planar crystals and graupel observed on 21 March 1973 at Wolf Creek Pass, Colorado (1452 MST–1558 MST).

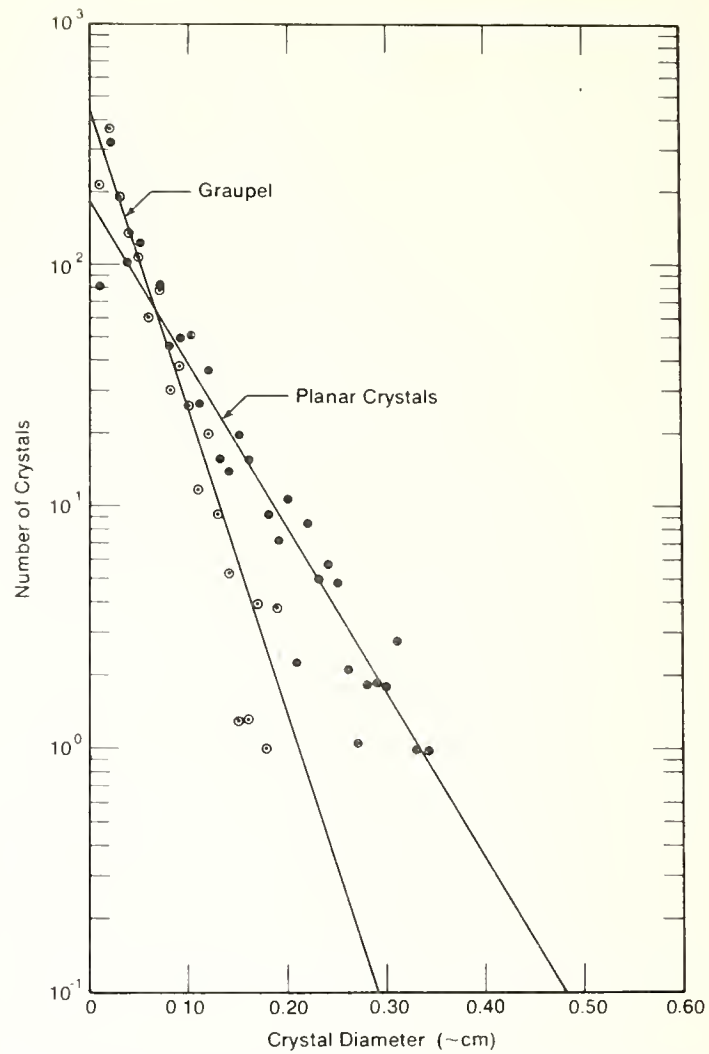


Figure 3. Distribution of planar crystals and graupel observed on 10 February 1973 at Wolf Creek Pass, Colorado (1748 MST–2027 MST).

3.2 ICE GROWTH AND SUBLIMATION

3.2.1 Unrimed Crystals

The growth rate of an unrimed planar crystal by deposition is

$$\cdot \frac{dm_u}{dt} \Big)_d = 4GS_iF_uD_u, \quad (4)$$

where

$$G = (L_s/R_rKT^2 + R_rT/e_iD)^{-1},$$

$$L_s = 2.83658(10^6),$$

$$K = 0.0243 + 0.00008(T - 273.16),$$

$$D = 2.26(T/273.16)^{1.81}(1/p),$$

$$R_v = 461.6,$$

$$e_i = 610.78 \exp \left[\frac{21.87456(T - 273.16)}{(T - 7.66)} \right],$$

and S_i is supersaturation with respect to a plane ice surface.

The ventilation factor in the depositional growth equation written in terms of Reynolds Number is

$$F_u = 1 + 0.22(R_v)^{1/2}. \quad (5)$$

The Reynolds Number for a planar crystal may, in turn, be expressed as a function of its dimensions, settling speed, and kinematic viscosity, or

$$R_v = 1.82r_u^{2/3}c_u^{1/3}V_u/\nu. \quad (6)$$

A mean value of $2(10^{-5}) \text{ m}^2 \text{ sec}^{-1}$ for the kinematic viscosity is selected as representative of cold orographic clouds. Observations of Auer and Veal (1970) show that the ratio of crystal radius to crystal thickness for planar crystals varies from about 5 for $r_u = 100$ microns to 30 for $r_u = 2500$ microns. We therefore assign to (6) an average value of 20. Finally, settling speeds for unrimed planar crystals are taken from Brown (1970) to be

$$V_u = 1.6834 D_u^{0.217}. \quad (7)$$

After substituting the above quantities into (6), the ventilation factor is

$$F_u = 1 + 36.96 D_u^{0.61}, \quad (8)$$

and (4) becomes,

$$\frac{dm_u}{dt} \Big|_a = 4GS_i D_u + 147.84GS_i D_u^{1.61}. \quad (9)$$

The growth of planar crystals by accretion is

$$\frac{dm_u}{dt} \Big|_a = EA\rho q_{cu} V_u. \quad (10)$$

The crystal cross-sectional area is given by $A = 0.64952 D_u^2$, and the crystal settling speed is given by (7). The mesoscale dynamical model predicts the mixing ratio of liquid cloud water (q_{cw}). The collection efficiency E of crystals for supercooled droplets is made a function of liquid cloud water content. This function accounts for the "collectability" of the liquid water present, and ranges from near zero for small droplets and low liquid water contents to a large percentage for large droplets and high liquid water contents (Fig. 4). The function is

$$E = 0.047 + 2274(\rho q_{cw}) - 1564000(\rho q_{cu})^2 \text{ for } (\rho q_{cu}) < 0.75(10^{-3}) \text{ kg m}^{-3}$$

and

$$E = 0.875 \text{ for } (\rho q_{cu}) \geq 0.75(10^{-3}) \text{ kg m}^{-3}. \quad (11)$$

Upon substituting the above quantities into (10) the equation for accretional growth becomes

$$\frac{dm_u}{dt} \Big|_a = 1.0934\rho q_{cu} E D_u^{2.217}. \quad (12)$$

The quantity of paramount interest is the production of ice by growth processes over the entire crystal population. To obtain this quantity, individual crystal growth rates are integrated over the total size distribution of crystals.

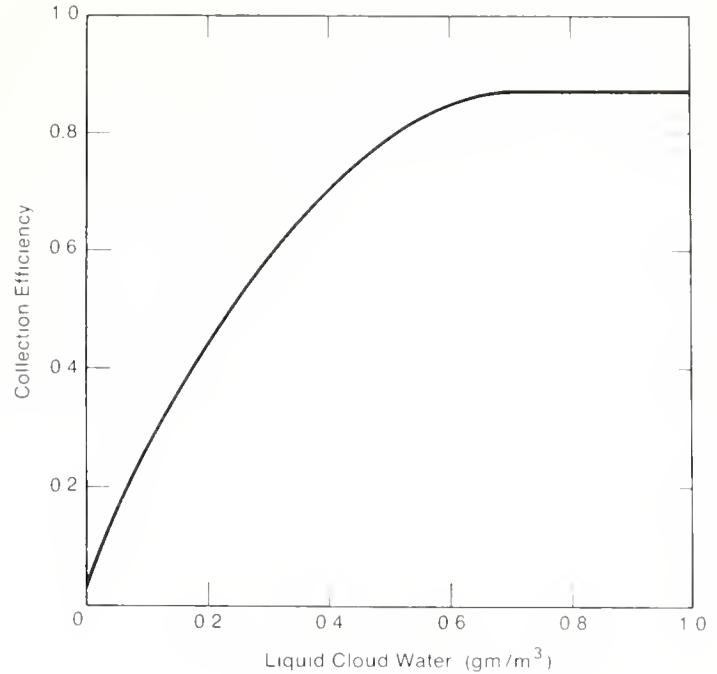


Figure 4. Efficiency of ice particles for collecting supercooled cloud water.

If the unrimed crystals are distributed according to a truncated Marshall-Palmer distribution, the production of total unrimed ice is

$$P_{qu} = \frac{1}{\rho} \int_0^{0.1} n_u e^{-\lambda_u D_u} \frac{dm_u}{dt} dD_u. \quad (13)$$

Substituting (9) and (12) into (13), the production of total unrimed ice is

$$\begin{aligned} P_{qu} = & (n_u/\rho) \left(4GS_i \int_0^{0.1} D_u e^{-\lambda_u D_u} dD_u \right. \\ & + 147.84GS_i \int_0^{0.1} D_u^{1.61} e^{-\lambda_u D_u} dD_u \\ & \left. + 1.0934 \rho q_{cu} E \int_0^{0.1} D_u^{2.217} e^{-\lambda_u D_u} dD_u \right). \end{aligned} \quad (14)$$

3.2.2 Partially Rimed Crystals

A similar set of growth equations can be derived for partially rimed crystals. The growth rate of partially rimed planar crystals by deposition is

$$\frac{dm_p}{dt} \Big|_d = 5GD_p F_p S_i. \quad (15)$$

The settling velocity of partially rimed crystals is taken from Jiusto (1967) to be

$$V_p = 6.796 D_p^{0.3}. \quad (16)$$

The ventilation factor for partially rimed crystals is derived similarly to (8) except in this case crystal radius is taken to be approximately ten times crystal thickness over a considerable size range. With this assumption the ventilation factor for partially rimed crystals becomes

$$F_p = 1 + 83.35 D_p^{0.65}. \quad (17)$$

Substituting (17) into (15), the depositional growth rate is

$$\frac{dm_p}{dt} \Big|_d = 5GS_i D_p + 416.75 GS_i D_p^{1.65}. \quad (18)$$

The growth rate of partially rimed planar crystals by accretion of supercooled droplets is

$$\frac{dm_p}{dt} \Big|_a = EA\rho q_{cw} V_p, \quad (19)$$

where E is defined by (11).

The same procedure used to develop (12) is followed, and upon substitution of (16) into (19) the growth rate by accretion becomes

$$\frac{dm_p}{dt} \Big|_a = 4.414 \rho q_{cw} E D_p^{2.3}. \quad (20)$$

Again the quantity of importance is the growth of ice over the entire partially rimed crystal distribution. The production of total ice by growth processes in this truncated Marshall-Palmer distribution is

$$P_{gp} = \frac{1}{\rho} \int_0^{0.1} n_p e^{-\lambda p} p^{D_p} \frac{dm_p}{dt} dD_p. \quad (21)$$

Substituting (18) and (20) into (21), the production of partially rimed ice is

$$\begin{aligned} P_{gp} = & (n_p / \rho) \left(5GS_i \int_0^{0.1} D_p e^{-\lambda p} p^{D_p} dD_p \right. \\ & + 416.75 GS_i \int_0^{0.1} D_p^{1.65} e^{-\lambda p} p^{D_p} dD_p \\ & \left. + 4.414 \rho q_{cw} E \int_0^{0.1} D_p^{2.3} e^{-\lambda p} p^{D_p} dD_p \right). \end{aligned} \quad (22)$$

3.2.3 Graupel

The growth rate of a graupel particle by deposition is

$$\frac{dm_g}{dt} \Big|_d = 6.2GD_g F_g S_i. \quad (23)$$

The settling velocity of graupel is taken from Nakaya and Terada (1934) to be

$$V_g = 76.18 D_g^{0.633}. \quad (24)$$

The ventilation factor for graupel is derived similarly to (8) except that, for this case, graupel is assumed to be spherical. The ventilation factor becomes with this assumption

$$F_g = 1 + 459.75 D_g^{0.82}. \quad (25)$$

Substituting (25) into (23), the depositional growth rate is

$$\frac{dm_g}{dt} \Big|_d = 6.2GD_g S_i + 2850.4GD_g^{1.82} S_i. \quad (26)$$

The growth rate of graupel by accretion is

$$\frac{dm_g}{dt} \Big|_a = EA\rho q_{cw} V_g, \quad (27)$$

where E is given by (11).

If we follow the same procedure used to develop (12), and substitute from (24) for the settling speed, (27) becomes

$$\frac{dm_g}{dt} \Big|_a = 59.83 \rho q_{cw} E D_g^{2.633}. \quad (28)$$

The quantity of importance is again the production of ice over the entire graupel distribution. If a truncated Marshall-Palmer distribution is assumed for graupel, the growth of graupel ice is

$$P_{gg} = \frac{1}{\rho} \int_0^{0.1} n_g e^{-\lambda g} p_g \frac{dm_g}{dt} dD_g. \quad (29)$$

Substituting (26) and (28) into (29), the total production of graupel ice is

$$\begin{aligned} P_{gg} = & (n_g / \rho) \left(6.2GS_i \int_0^{0.1} D_g e^{-\lambda g} p_g dD_g \right. \\ & + 2850.4GS_i \int_0^{0.1} D_g^{1.82} e^{-\lambda g} p_g dD_g \\ & \left. + 59.83 \rho q_{cw} E \int_0^{0.1} D_g^{2.633} e^{-\lambda g} p_g dD_g \right). \end{aligned} \quad (30)$$

3.3. SEDIMENTATION AND FLUX DIVERGENCE

3.3.1 Unrimed Crystals

The vertical flux of unrimed crystals relative to the updraft is

$$F_{up} = \int_0^{0.01} n_u V_u e^{-\lambda_u p_u} dD_u. \quad (31)$$

Substituting for V_u from (7), the vertical flux of unrimed crystals due to sedimentation is

$$F_{up} = \int_0^{0.01} 1.6834 n_u D_u^{0.217} e^{-\lambda_u p_u} dD_u. \quad (32)$$

The production of ice particles due to sedimentation is obtained next by differentiating the flux of particles with height, or

$$C_{us} = \frac{\partial}{\partial z} \int_0^{0.01} 1.6834 n_u D_u^{0.217} e^{-\lambda_u p_u} dD_u. \quad (33)$$

Crystals are carried along with the vector wind, which is predicted by the mesoscale dynamical model. The production of unrimed particles due to flux divergence is then

$$C_{ud} = -\frac{\partial}{\partial x} (N_u u) - \frac{\partial}{\partial y} (N_u v) - \frac{\partial}{\partial z} (N_u w). \quad (34)$$

The vertical flux of ice in the form of unrimed crystals relative to the updraft is

$$F_{ur} = \int_0^{0.01} n_u m_u V_u e^{-\lambda_u p_u} dD_u. \quad (35)$$

Substituting from (7) again for V_u , and using the empirical relationship of Nakaya and Terada (1934) for unrimed crystals ($m_u = 0.0038 D_u^2$) to convert from crystal mass to size, the vertical flux of ice due to sedimentation is

$$F_{ur} = \int_0^{0.01} 0.0064 n_u D_u^{2.217} e^{-\lambda_u p_u} dD_u. \quad (36)$$

The production of ice in the form of unrimed crystals due to sedimentation is obtained by differentiating the flux of ice with height, or in terms of unit mass

$$P_{us} = \frac{\partial}{\partial z} \int_0^{0.01} (0.0064/\rho) n_u D_u^{2.217} e^{-\lambda_u p_u} dD_u. \quad (37)$$

The production of unrimed ice due to flux divergence is then

$$P_{ud} = -\frac{\partial}{\partial x} (q_u u) - \frac{\partial}{\partial y} (q_u v) - \frac{\partial}{\partial z} (q_u w). \quad (38)$$

3.3.2 Partially Rimed Crystals

The vertical flux of partially rimed crystals relative to the updraft is

$$F_{pr} = \int_0^{0.01} n_p V_p e^{-\lambda_p p_p} dD_p. \quad (39)$$

Substituting for V_p from (16), the vertical flux of particles due to sedimentation is

$$F_{pp} = \int_0^{0.01} 6.796 n_p D_p^{0.3} e^{-\lambda_p p_p} dD_p. \quad (40)$$

The production of partially rimed ice particles by sedimentation is obtained next by differentiating the flux of particles with height, or

$$C_{ps} = \frac{\partial}{\partial z} \int_0^{0.01} 6.796 n_p D_p^{0.3} e^{-\lambda_p p_p} dD_p. \quad (41)$$

Production of partially rimed crystals due to flux divergence is then

$$C_{pd} = -\frac{\partial}{\partial x} (N_p u) - \frac{\partial}{\partial y} (N_p v) - \frac{\partial}{\partial z} (N_p w). \quad (42)$$

The vertical flux of ice in the form of partially rimed crystals relative to the updraft is

$$F_{pr} = \int_0^{0.01} n_p m_p V_p e^{-\lambda_p p_p} dD_p. \quad (43)$$

Using the empirical relationship of Nakaya and Terada (1934) for partially rimed crystals ($m_p = 0.027 D_p^2$) to convert from crystal mass to size and substituting again from (16) for V_p , the vertical flux of ice due to sedimentation is

$$F_{pr} = \int_0^{0.01} 0.1835 n_p D_p^{2.3} e^{-\lambda_p p_p} dD_p. \quad (44)$$

The production of partially rimed ice due to sedimentation is obtained by differentiating the flux of ice with height, or in terms of unit mass

$$P_{ps} = \frac{\partial}{\partial z} \int_0^{0.1} (0.1835/\rho) n_p D_p^{2.3} e^{-\lambda_p D_p} dD_p. \quad (45)$$

The production of partially rimed ice due to flux divergence is then

$$P_{pd} = -\frac{\partial}{\partial x} (q_p u) - \frac{\partial}{\partial y} (q_p v) - \frac{\partial}{\partial z} (q_p w). \quad (46)$$

3.3.3 Graupel

The vertical flux of graupel particles relative to the updraft is

$$F_{qp} = \int_0^{0.1} n_q V_g e^{-\lambda_q D_g} dD_g. \quad (47)$$

Substituting for V_g from (24), the vertical flux of graupel particles due to sedimentation is

$$F_{qs} = \int_0^{0.1} 76.18 n_q D_q^{0.633} e^{-\lambda_q D_g} dD_g. \quad (48)$$

The production of graupel particles by sedimentation is obtained next by differentiating the flux of particles with height, or

$$C_{qs} = \frac{\partial}{\partial z} \int_0^{0.1} 76.18 n_q D_q^{0.633} e^{-\lambda_q D_g} dD_g. \quad (49)$$

Production of graupel particles due to flux divergence is then

$$C_{qd} = -\frac{\partial}{\partial x} (N_q u) - \frac{\partial}{\partial y} (N_q v) - \frac{\partial}{\partial z} (N_q w). \quad (50)$$

The vertical flux of graupel ice relative to the updraft is

$$F_{gi} = \int_0^{0.1} n_q m_g V_g e^{-\lambda_q D_g} dD_g. \quad (51)$$

The empirical relationship of Nakaya and Terada (1934) for graupel, $m_g = 65D_g^3$, is used to convert from graupel mass to size. Substituting this relationship into (51), the vertical flux of graupel ice due to sedimentation is

$$F_{qi} = \int_0^{0.1} 4951.7 n_q D_q^{3.633} e^{-\lambda_q D_g} dD_g. \quad (52)$$

The production of graupel ice due to sedimentation is obtained by differentiating the flux of ice with height, or in terms of unit mass

$$P_{qs} = \frac{\partial}{\partial z} \int_0^{0.1} (4951.7/\rho) n_q D_q^{3.633} e^{-\lambda_q D_g} dD_g. \quad (53)$$

The production of graupel ice due to flux divergence is then

$$P_{qd} = -\frac{\partial}{\partial x} (q_g u) - \frac{\partial}{\partial y} (q_g v) - \frac{\partial}{\partial z} (q_g w). \quad (54)$$

3.4 ELIMINATION OF ICE PARTICLES BY SUBLIMATION

3.4.1 Unrimed Crystals

The sublimation rate for small unrimed crystals, for which ventilation effects are negligible, is from (9)

$$\frac{dm_u}{dt} = 4GS_i D_u. \quad (55)$$

If the Nakaya and Terada (1934) expression that relates unrimed crystal mass and size is differentiated, we obtain

$$dm_u = 0.0076 D_u dD_u. \quad (56)$$

Substituting (56) into (55) and integrating over a time step of the model, Δt , as crystal diameter reduces from D_{us} to zero, we obtain

$$\int_{D_{us}}^0 dD_u = \int_{\Delta t} (4GS_i/0.0076) dt. \quad (57)$$

Performing the integration and simplifying, we obtain

$$D_{us} = -526.31 GS_i \Delta t, \quad (58)$$

where D_{us} is the diameter of a crystal that will just sublime away during a model time step. Clearly, crystals of a smaller diameter will also sublime entirely.

If we integrate the truncated Marshall-Palmer distribution with respect to crystal diameter from zero to D_{us} , we obtain an expression for the number of unrimed crystals that disappear through sublimation during a model time step, or

$$N_{us} = \int_0^{D_{us}} n_u e^{-\lambda_u D_u} dD_u. \quad (59)$$

3.4.2 Partially Rimed Crystals

The sublimation rate for small partially rimed crystals, for which ventilation effects are negligible, is taken from (18) to be

$$\frac{dm_p}{dt} = 5GS_i D_p. \quad (60)$$

If the relationship of Nakaya and Terada (1934) that converts partially rimed crystal mass to size is differentiated, we obtain

$$dm_p = 0.054 D_p dD_p. \quad (61)$$

Substituting (61) into (60), and integrating over a time step of the model as crystal diameter reduces from D_{ps} to zero, we obtain

$$\int_{D_{ps}}^0 dD_p = \int_{\Delta t} (5GS_i / 0.054) dt. \quad (62)$$

Performing the integration and simplifying, we obtain

$$D_{ps} = -92.59GS_i \Delta t, \quad (63)$$

where D_{ps} is the diameter of a partially rimed crystal that just sublimates entirely during a model time step.

If we integrate the truncated Marshall-Palmer distribution with respect to crystal diameter from zero to D_{ps} , we obtain an expression for the number of partially rimed crystals eliminated by sublimation during a model time step, or

$$N_{ps} = \int_0^{D_{ps}} n_p e^{-\lambda_p D_p} dD_p. \quad (64)$$

3.4.3 Graupel

The sublimation rate for small graupel particles is from (26)

$$\frac{dm_g}{dt} = 6.2GD_g S_i. \quad (65)$$

We differentiate the empirical relationship of Nakaya and Terada (1934) that converts graupel mass to size to obtain

$$dm_g = 195D_g^2 dD_g. \quad (66)$$

Substituting (66) into (65) and integrating over a time step of the model as graupel diameter reduces from D_{gs} to zero, we obtain

$$\int_{D_{gs}}^0 dD_g = \int_{\Delta t} (6.2GS_i / 195) dt. \quad (67)$$

Performing the integration and simplifying, we obtain

$$D_{gs} = (-0.0636GS_i \Delta t)^{1/2}, \quad (68)$$

where D_{gs} is the diameter of graupel that will just sublimate during a model time step.

The truncated Marshall-Palmer distribution is integrated with respect to diameter from zero to D_{gs} to obtain an expression for the number of graupel particles that are eliminated by sublimation during a model time step. Thus

$$N_{gs} = \int_0^{D_{gs}} n_g e^{-\lambda_g D_g} dD_g. \quad (69)$$

3.5 CONVERSION FUNCTIONS

3.5.1 Transfer of Unrimed to Partially Rimed Crystals

A conversion from unrimed crystals to partially rimed crystals is assumed when the accretional growth rate of a crystal attains a specified factor, f_1 , of the depositional growth rate.

From (9) and (12), this conversion condition can be expressed as

$$\begin{aligned} f_1 (4GS_i D_c + 147.84GS_i D_c^{1.61}) \\ = 1.0934\rho q_{ew} E D_c^{2.217}. \end{aligned} \quad (70)$$

If we let $y = D_c^{0.61}$, then to good approximation (70) can be written as a quadratic equation in y . This equation can then be solved to obtain an expression for the crystal diameter that satisfies the conversion criteria. The general form of the solution is

$$D_c = \left[\frac{147.84GS_i f_1}{2.1868\rho q_{ew} E} \right]^{1/6.39} + \frac{\sqrt{21856.7 (GS_i f_1)^2 + 17.5 GS_i \rho q_{ew} E f_1}}{2.1868\rho q_{ew} E} \quad (71)$$

Solutions for (71) are shown in Figure 5 for $f_1=1$, which is the factor presently used in the microphysical model.

After defining the crystal diameter that satisfies the conversion criteria, those crystals in the distribution with diameters larger than D_c are transferred to the partially rimed category. The number of such crystals is defined by integrating the truncated Marshall-Palmer distribution with respect to crystal diameter over sizes greater than D_c , or

$$N_{up} = \int_{D_c}^{0.01} n_u e^{-\lambda_u D_u} dD_u, \quad (72)$$

and $N_{up}=0$ if $D_c > 0.01$.

The mass of ice to be transferred to the partially rimed category (or the mass of ice in crystals with diameters greater than D_c and less than 0.01 meters) is

$$q_{up} = (0.0038/\rho) \int_{D_c}^{0.01} n_u D_u^2 e^{-\lambda_u D_u} dD_u. \quad (73)$$

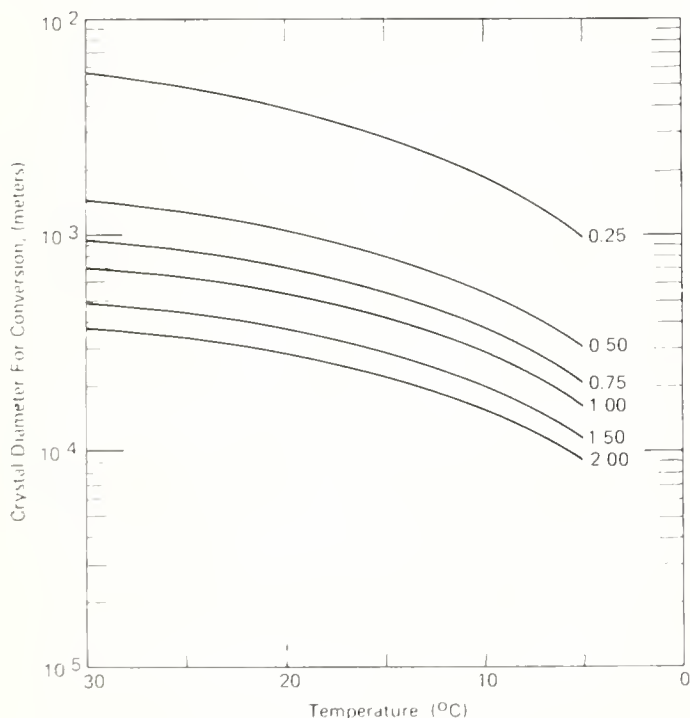


Figure 5. Crystal diameter for conversion of unrimmed crystals to partially rimed crystals as a function of environmental temperature and cloud liquid water content (gm m^{-3}).

3.5.2 Transfer of Partially Rimed Crystals to Graupel

A conversion from partially rimed crystals to graupel is assumed when the accretional growth rate of a crystal reaches a specified factor, f_2 , of the depositional growth rate.

Using (18) and (20), this conversion criterion can be expressed

$$\begin{aligned} f_2 (5GS_i D_d + 416.75GS_i D_d^{1.65}) \\ = 4.414\rho q_{cw} ED\eta^3. \end{aligned} \quad (74)$$

If we let $y = D_d^{0.65}$, then (74) can be solved as a quadratic equation in y . An expression can then be obtained for the crystal diameter that satisfies the conversion criterion, or

$$\begin{aligned} D_d = \left[\frac{416.75GS_i f_2}{8.828\rho q_{cw} E} \right. \\ \left. + \frac{\sqrt{173680 (GS_i f_2)^2 + 88.28GS_i \rho q_{cw} E f_2}}{8.828\rho q_{cw} E} \right]^{1.538}. \end{aligned} \quad (75)$$

Solutions for (75) are shown in Figure 6 for $f_2=7$, which is the factor currently used in the microphysical model.

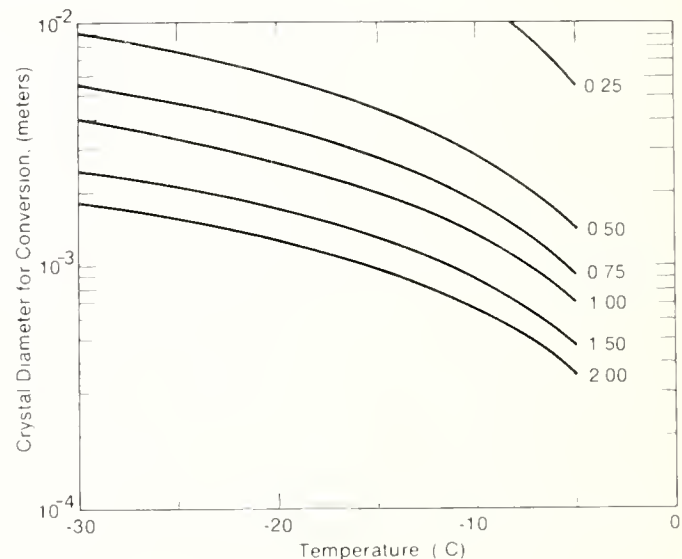


Figure 6. Crystal diameter for conversion of partially rimed crystals to graupel as a function of environmental temperature and cloud liquid water content (gm m^{-3}).

The number of crystals to be transferred each model time step is defined by integrating the truncated Marshall-Palmer distribution with respect to crystal diameter from D_d to 0.01, or

$$N_{pg} = \int_{D_d}^{0.01} n_p e^{-\lambda_p D_p} dD_p. \quad (76)$$

The mass of ice to be transferred to graupel is then

$$q_{pg} = (0.027/\rho) \int_{D_d}^{0.01} n_p D_p^2 e^{-\lambda_p D_p} dD_p. \quad (77)$$

3.6 PREDICTION EQUATIONS

3.6.1 Unrimed Crystals

A prediction equation for the mixing ratio of ice in the form of unrimed crystals is formulated by combining the production terms (3), (14), (37), and (38), or

$$\begin{aligned} \frac{\partial q_u}{\partial t} &= \frac{m_u}{\rho} \frac{\partial N_u}{\partial T} \frac{dT}{dt} \\ &+ (n_u/\rho) \left[4GS_i \int_0^{0.01} D_u e^{-\lambda_u D_u} dD_u \right. \\ &+ 147.84GS_i \int_0^{0.01} D_u^{1.61} e^{-\lambda_u D_u} dD_u \\ &\left. + 1.0934\rho q_{cr} E \int_0^{0.01} D_u^{2.217} e^{-\lambda_u D_u} dD_u \right] \\ &+ \frac{\partial}{\partial z} \int_0^{0.01} (0.0064/\rho) n_u D_u^{2.217} e^{-\lambda_u D_u} dD_u \\ &- \frac{\partial}{\partial x} (q_u u) - \frac{\partial}{\partial y} (q_u v) - \frac{\partial}{\partial z} (q_u w). \end{aligned} \quad (78)$$

The mixing ratio of unrimed ice at time n is obtained from the centered finite difference equation

$$q_u^n = q_u^{n-2} + 2\Delta t \frac{\partial q_u}{\partial t} \Big|^{n-1}. \quad (79)$$

The value q_u^n is then adjusted by subtracting q_{up}^n , the unrimed mixing ratio to be transferred to the partially rimed category at time n , so that

$$q_u^n = q_u^n - q_{up}^n. \quad (80)$$

The prediction equation for the concentration of unrimed crystals is obtained by combining the production terms (2), (33), and (34), or

$$\begin{aligned} \frac{\partial N_u}{\partial t} &= \frac{\partial N_u}{\partial T} \frac{dT}{dt} + \frac{\partial}{\partial z} \int_0^{0.01} 1.6834 n_u D^{0.217} e^{-\lambda_u D_u} dD_u \\ &- \frac{\partial}{\partial x} (N_u u) - \frac{\partial}{\partial y} (N_u v) - \frac{\partial}{\partial z} (N_u w). \end{aligned} \quad (81)$$

The concentration of unrimed ice crystals at time n is obtained from

$$N_u^n = N_u^{n-2} + 2\Delta t \frac{\partial N_u}{\partial t} \Big|^{n-1}. \quad (82)$$

The value N_u^n is then adjusted by subtracting the number of unrimed crystals that sublimated or that were transferred to the partially rimed category at time n . The adjusted value is then

$$N_u^n = N_u^n - N_{us}^n - N_{up}^n. \quad (83)$$

3.6.2 Partially Rimed Crystals

A prediction equation for the mixing ratio of ice in the form of partially rimed crystals is formulated by combining the production terms (22), (45) and (46), or

$$\begin{aligned} \frac{\partial q_p}{\partial t} &= (n_p/\rho) \left[5GS_i \int_0^{0.01} D_p e^{-\lambda_p D_p} dD_p \right. \\ &+ 416.75GS_i \int_0^{0.01} D_p^{1.65} e^{-\lambda_p D_p} dD_p \\ &\left. + 4.414\rho q_{cr} E \int_0^{0.01} D_p^{2.3} e^{-\lambda_p D_p} dD_p \right] \\ &+ \frac{\partial}{\partial z} \int_0^{0.01} (0.1835/\rho) n_p D_p^{2.3} e^{-\lambda_p D_p} dD_p \\ &- \frac{\partial}{\partial x} (q_p u) - \frac{\partial}{\partial y} (q_p v) - \frac{\partial}{\partial z} (q_p w). \end{aligned} \quad (84)$$

The mixing ratio of partially rimed ice at time n is obtained from

$$q_p^n = q_p^{n-2} + 2\Delta t \frac{\partial q_p}{\partial t} \Big|^{n-1}. \quad (85)$$

The value of q_p^n is adjusted by adding the mass transferred from the unrimed category and subtracting the mass transferred to graupel at time n , so that

$$q_p^n = q_p^{n*} + q_{up}^n - q_{pg}^n. \quad (86)$$

A prediction equation for the concentration of partially rimed crystals can be formulated by combining the production terms (41) and (42), or

$$\begin{aligned} \frac{\partial N_p}{\partial t} &= \frac{\partial}{\partial z} \int_0^{0.1} 6.796 n_p D_p^{0.3} e^{-\lambda_p D_p} dD_p \\ &- \frac{\partial}{\partial x} (N_p u) - \frac{\partial}{\partial y} (N_p v) - \frac{\partial}{\partial z} (N_p w). \end{aligned} \quad (87)$$

The concentration of partially rimed ice crystals at time n is obtained from

$$N_p^{n*} = N_p^{n-2} + 2\Delta t \frac{\partial N_p}{\partial t} \Big|^{n-1}. \quad (88)$$

The value of N_p^{n*} is adjusted by subtracting the number of partially rimed ice crystals that have sublimated during the time step or that were transferred to the graupel category, and adding the crystals transferred in from the unrimed category. The unadjusted value is then

$$N_p^n = N_p^{n*} + N_{up}^n - N_{ps}^n - N_{pg}^n. \quad (89)$$

3.6.3 Graupel

A prediction equation for the graupel mixing ratio is formulated by combining the production terms (30), (53) and (54), or

$$\begin{aligned} \frac{\partial q_g}{\partial t} &= (n_g/\rho) \left[6.2 GS_t \int_0^{0.1} D_g^{2.633} e^{-\lambda_g D_g} dD_g \right. \\ &+ 2850.4 GS_t \int_0^{0.1} D_g^{1.82} e^{-\lambda_g D_g} dD_g \\ &\left. + 59.83 \rho q_{eu} E \int_0^{0.1} D_g^{2.633} e^{-\lambda_g D_g} dD_g \right] \\ &+ \frac{\partial}{\partial z} \int_0^{0.1} (4951.7/\rho) n_g D_g^{3.633} e^{-\lambda_g D_g} dD_g \\ &- \frac{\partial}{\partial x} (q_g u) - \frac{\partial}{\partial y} (q_g v) - \frac{\partial}{\partial z} (q_g w). \end{aligned} \quad (90)$$

The mixing ratio of graupel at time n is obtained from

$$q_g^{n*} = q_g^{n-2} + 2\Delta t \frac{\partial q_g}{\partial t} \Big|^{n-1}. \quad (91)$$

The value of q_g^{n*} is adjusted by adding the mass transferred in from the partially rimed category, or

$$q_g^n = q_g^{n*} + q_{pg}^n. \quad (92)$$

A prediction equation for the concentration of graupel can be formulated by combining the production terms (49) and (50), or

$$\begin{aligned} \frac{\partial N_g}{\partial t} &= \frac{\partial}{\partial z} \int_0^{0.1} 76.18 n_g D_g^{0.633} e^{-\lambda_g D_g} dD_g \\ &- \frac{\partial}{\partial x} (N_g u) - \frac{\partial}{\partial y} (N_g v) - \frac{\partial}{\partial z} (N_g w). \end{aligned} \quad (93)$$

The concentration of graupel particles at time n is obtained from

$$N_g^n = N_g^{n-2} + 2\Delta t \frac{\partial N_g}{\partial t} \Big|^{n-1}. \quad (94)$$

The value of N_g^{n*} is adjusted by subtracting the number of graupel particles that sublimate during the model time step and adding the particles transferred from the partially rimed category, or

$$N_g^n = N_g^{n*} - N_{gs}^n + N_{pg}^n. \quad (95)$$

4. DYNAMICAL MODEL AND INITIAL CONDITIONS

4.1 CHARACTERISTICS OF THE DYNAMICAL MODEL

The mesoscale dynamical model in which these microphysical equations are merged is explained in detail by Nickerson and Magaziner (1976) so only a brief summary follows here. This Primitive Equation mesoscale model employs a modified Sigma system as the vertical coordinate. The modification of the Sigma system gives greater resolution in the boundary layer. A constant flux layer is assumed between the surface and the first grid point above (approximately 18 meters above ground). Eddy exchange coefficients in this layer are obtained from the Bussinger-Dyer surface layer formulation (Deardorff, 1972).

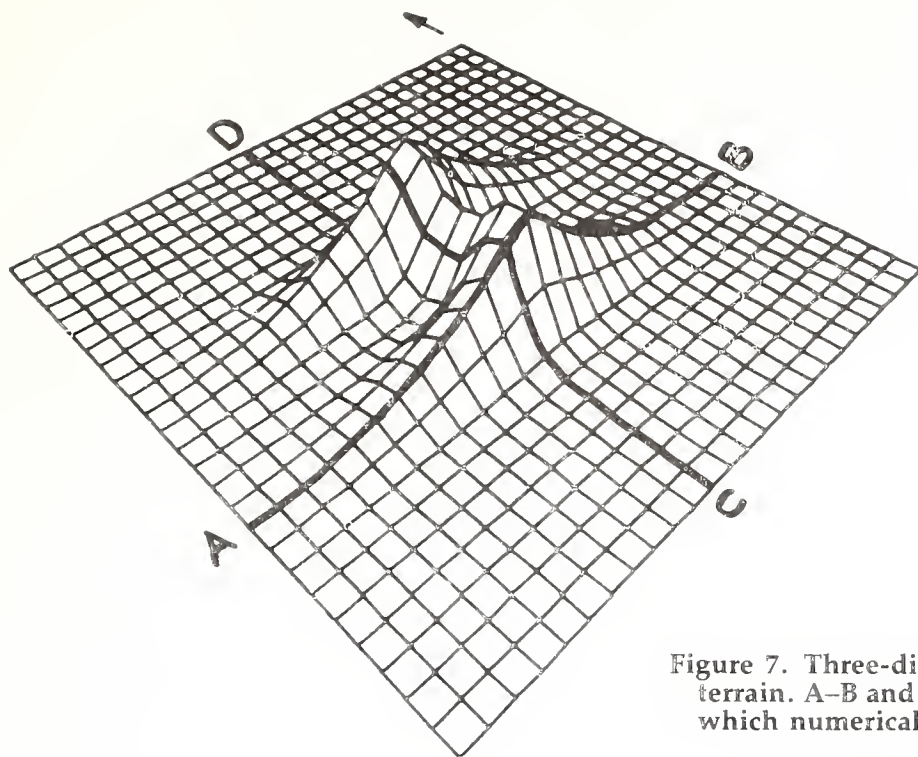


Figure 7. Three-dimensional perspective of model terrain. A-B and C-D are the cross-sections along which numerical results are presented.

A boundary layer above the constant flux layer extends upward to one kilometer and an O'Brien profile specifies the eddy exchange coefficients in this layer. Staggered grids are used on a Sigma surface so that u and v are defined on one grid system while thermodynamic variables are defined on another. The vertical motion parameter is defined at points between the Sigma surfaces. Centered differences are used to represent the time derivative, except that at every fifth time-step a time-and-space uncentered Matsuno procedure (Arakawa and Mintz, 1974) is introduced. A smoothing operator is applied to predicted fields of velocity to suppress $2\Delta x$ noise. The horizontal domain of the mesoscale model is 250 km by 250 km with a grid size of 10 km. The time-step is currently 15 seconds.

At the upper boundary the time derivative of Sigma is set to zero. Winds and temperature at the upper boundary are set equal to values at the grid point below. A viscous term is added to the predictive equations for velocity on the lateral and top boundaries, specifically at the first two interior grid points. Thermodynamic variables are specified at all boundaries; winds are specified on inflow boundaries and extrapolated from interior values on outflow boundaries.

4.2 TOPOGRAPHY

An isolated complex mountain massif was chosen for initial model runs. This had the advantage of maintaining rather simple boundary conditions while the behavior of microphysical processes is investigated. The terrain chosen (Fig. 7) is a twin-peaked large mountain massif generated by the following mathematical function (a superposition of three Gaussian functions):

$$z(x, y) = a_0 \{ \exp [a_1(x - x_0)^2 + a_2(y - y_0)^2] \\ \exp [a_1(x - x_0)^2 + a_2(y + y_0)^2] \} \\ + a_3 \exp [a_4(x - x_0)^2 + a_5 y^2],$$

where $a_0 = 1.6 \times 10^3$, $a_1 = -3.7836 \times 10^{-10}$, $a_2 = -0.532 \times 10^{-8}$, $a_3 = 1.4382 \times 10^3$, $a_4 = -0.5204 \times 10^{-8}$, $a_5 = -1.0284 \times 10^{-9}$, $x_0 = 1.3 \times 10^5$, $y_0 = 2.823 \times 10^4$, and all distances are expressed in meters.

The shape of the mountain is identical (except for a vertical scale exaggeration) to that reported on by Lin et al. (1974). The mountain massif rises from a plain that is 1500 meters above sea level, and reaches 3640 meters at the top of the twin peaks.

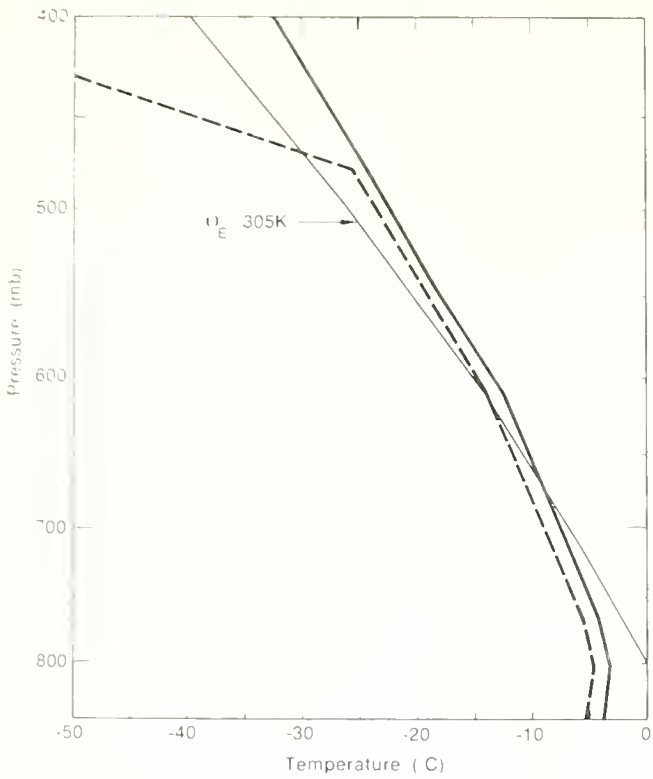


Figure 8. Sounding of temperature (solid line) and dew point temperature (dashed line) used for initializing mesoscale model. Moist layer is at 90% relative humidity.

4.3 INITIAL CONDITIONS

The temperature and moisture sounding used to initialize the model is depicted in Figure 8. Note that the sounding is stable with temperature lapse rates less than the moist adiabatic lapse rate. The very stable layer next to the surface is frequently observed in the Rocky Mountain area. The atmosphere is moist (90% relative humidity) up to about 480 mb, and the temperature at this level is approximately -25°C. Some lifting is therefore required to saturate the airmass and cause the development of clouds. A uniform westerly wind of 5 m sec⁻¹ is used.

The dynamical and microphysical prediction equations were started simultaneously and the model integrated for 4500 seconds. Output from these prediction equations at certain points during the integration are presented next.

5. NUMERICAL RESULTS

In Figures 9 through 13 results are displayed for a west-east cross-section (along the wind) through the south peak, and also for a south-north cross-section (normal to the wind) located 10 km, or one grid point, upwind of the twin peaks. (Locations of these cross-sections are depicted in Fig. 7.)

The vertical motion profile for a section along the wind at 600 seconds is shown in Figure 9. Vertical motion exceeds 10 cm sec⁻¹ upwind of the crest and -10 cm sec⁻¹ downwind of the peak. The upwind area of positive vertical motion slopes slightly downward toward the crest.

Using the definition that cloud exists when the liquid water mixing ratio (q_{cw}) equals or exceeds 0.01 gm kgm⁻¹, note in Figure 10 that three blobs of cloud water have formed after 600 seconds. These are located upwind of the peak, one at low level and two near the top of the moist layer. The locations of these initial cloud parcels are important, since ice nucleation occurs in the model when supercooled clouds undergo further cooling.

Figure 11 depicts the vertical motion field at 1200 seconds into the integration. Although there are minor changes in the field since 600 seconds, the basic features remain relatively unchanged. The liquid water cloud at 1200 seconds into the run is shown in Figure 12. The lower cloud just above the upwind slope has continued to develop and now has a $q_{cw} \geq 0.10$ gm kgm⁻¹. One of the initial high-level cloud parcels persists, while the other has disappeared. It is evident from the total ice mixing ratio (q_i) at 1200 seconds (Fig. 13) that the latter parcel was converted to ice through glaciation. Note that $q_i > 0.05$ gm kgm⁻¹ in this area.

Mixing ratios of cloud water and total ice at 1200 seconds normal to the wind flow are shown in Figures 14 and 15. Note that $q_{cw} > 0.20$ gm kgm⁻¹ in the saddle area between the peaks, while $q_i > 0.05$ gm kgm⁻¹ at the 6 km level just to the saddle side of the twin peaks.

At 2400 seconds into the run, Figures 16 and 17 indicate that cloud water has continued to grow in the lower part of the orographic cloud, while substantial ice growth has glaciated the

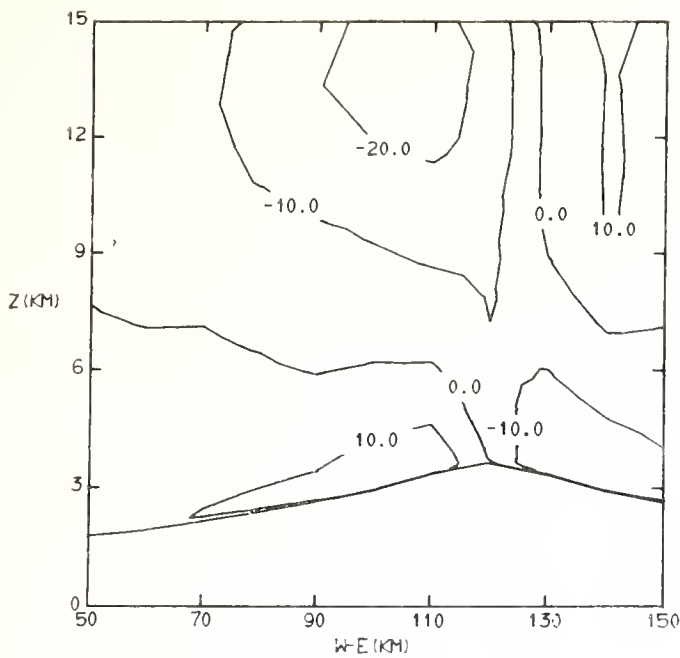


Figure 9. Vertical motion (cm sec^{-1}) along the wind at 600 seconds into the integration.

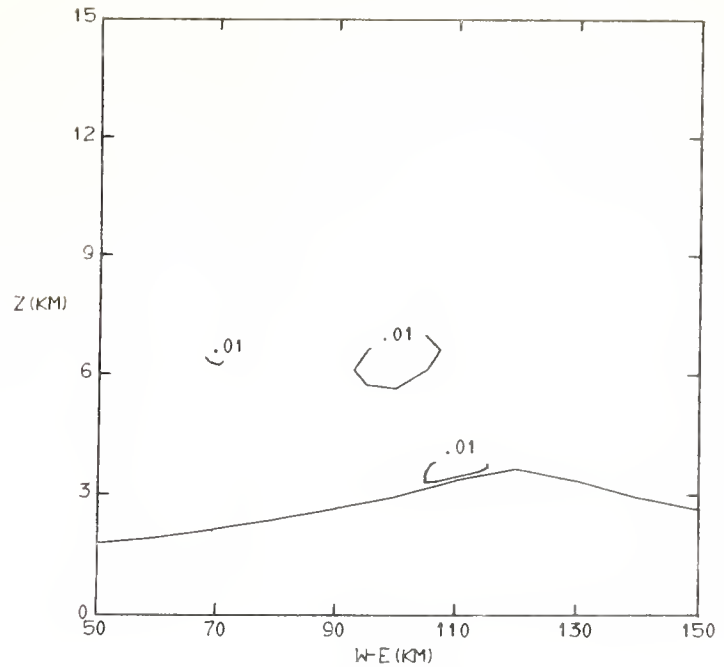


Figure 10. Mixing ratio of cloud water (gm kgm^{-1}) along the wind at 600 seconds into the integration.

upper portion of the cloud. The mixing ratio of cloud water has increased to above 0.30 gm kgm^{-1} in the lowest levels just upwind of the crest; the mixing ratio of total ice exceeds 0.20 gm kgm^{-1} in middle sections of the cloud just upwind of the peaks. Note that the 0.01 gm kgm^{-1} contour for q_i reaches the mountain top and snow is now falling on the peaks. From Figures 18, 19, and 20 it is evident that this first snowfall

is mostly in the form of graupel. Note that the 0.01 gm kgm^{-1} contours for unrimed ice (q_u) and partially rimed ice (q_p) are still suspended above the peaks, while the graupel mixing ratio (q_g) has reached 0.05 gm kgm^{-1} on the upwind surface. Also, note how unrimed ice is being carried over the crest by the westerly wind flow, and how the two original ice nucleating cells remain distinct entities while growing with time.

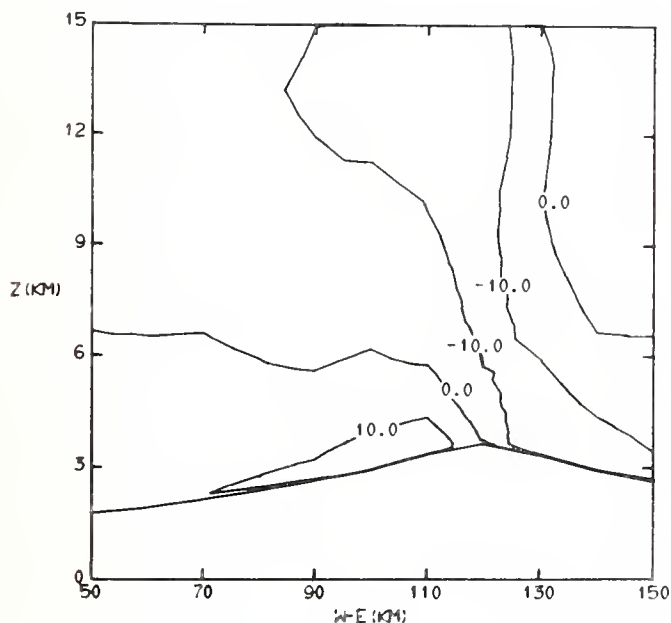


Figure 11. Vertical motion (cm sec^{-1}) along the wind at 1200 seconds into the integration

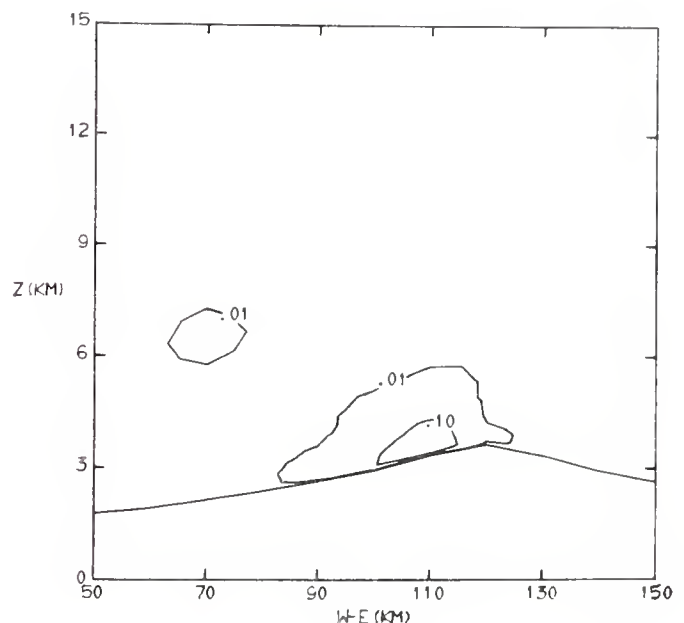


Figure 12. Mixing ratio of cloud water (gm kgm^{-1}) along the wind at 1200 seconds into the integration.

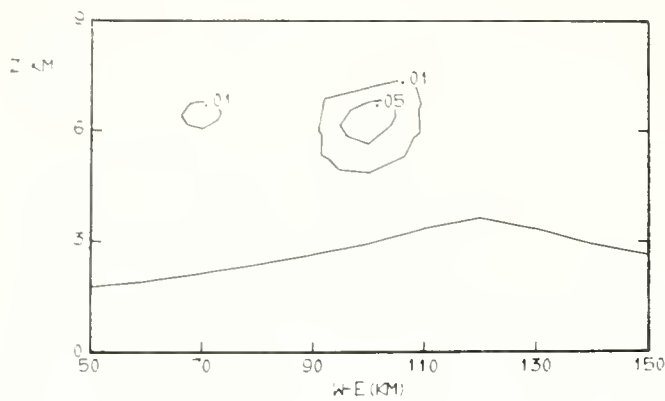


Figure 13. Mixing ratio of total ice (gm kgm^{-1}) along the wind at 1200 seconds into the integration.

Cross-sections normal to the wind at 2400 seconds (Figs. 21–25) show that cloud water has increased to over 0.40 gm kgm^{-1} in the saddle area between the peaks. Total ice exceeds 0.30 gm kgm^{-1} at about the 5-km level and just to the saddle side of the peaks. Nearly all ice above 5 km is in the form of unrimed crystals. Partially rimed crystals and graupel make up most of the ice over the peaks below 4.5 km.

At 3750 seconds into the run some interesting changes are apparent. Note in Figure 26 that cloud water has been depleted near the summit, and the 0.30 gm kgm^{-1} contour displaced further down the upwind slope. The reason for this is evident in Figures 27–30, which show that substantial quantities of cloud water have been converted to ice near the summit. Total ice in excess of 0.30 gm kgm^{-1} is now present near the peaks, and is composed mainly of partially rimed crystals and graupel. Unrimed crystals have now reached the mountain sum-

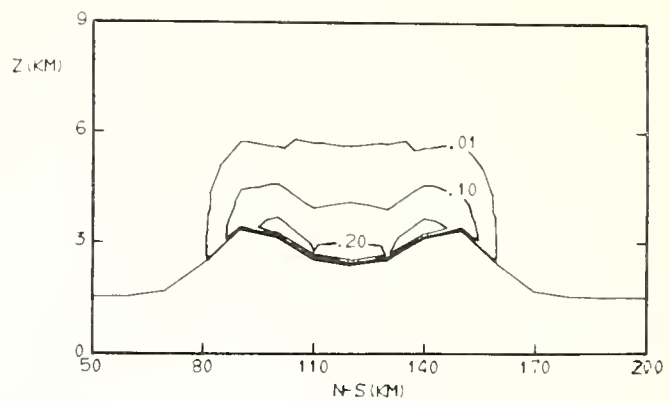


Figure 14. Mixing ratio of cloud water (gm kgm^{-1}) normal to the wind at 1200 seconds into the integration.

mit, but many continue to be carried over the crest to the leeward side.

Cross-sections normal to the wind at 3750 seconds (Figs. 31–35) show that cloud water has decreased to 0.30 gm kgm^{-1} in the saddle area. Cloud water has also been considerably depleted on the upwind flanks of the high peaks. Conversely, total ice has increased to near 0.40 gm kgm^{-1} at the 4.5-km to 5-km level above the peaks, and also near the surface on the saddle side of the peaks. The maximum of total ice at high levels is largely due to unrimed crystals, whereas partially rimed crystals contribute most to the lower maximum. Graupel has decreased over the peaks as cloud water has been depleted, but continues to increase over the saddle area.

At the end of the run, or 4500 seconds, cloud water in excess of 0.30 gm kgm^{-1} has been displaced even further down the upwind slope (Fig. 36). The two original maxima in total ice,

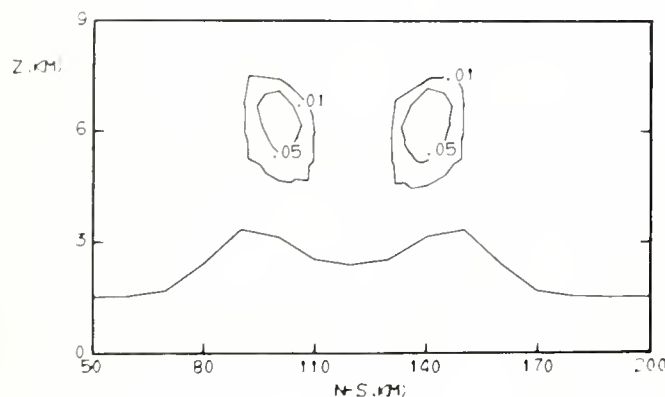


Figure 15. Mixing ratio of total ice (gm kgm^{-1}) normal to the wind at 1200 seconds into the integration.

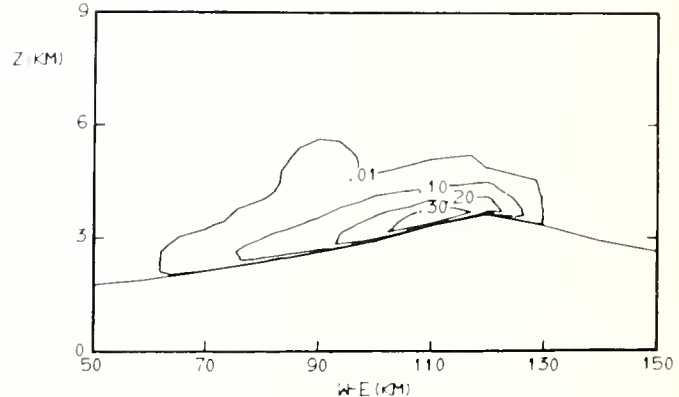


Figure 16. Mixing ratio of cloud water (gm kgm^{-1}) along the wind at 2400 seconds into the integration.

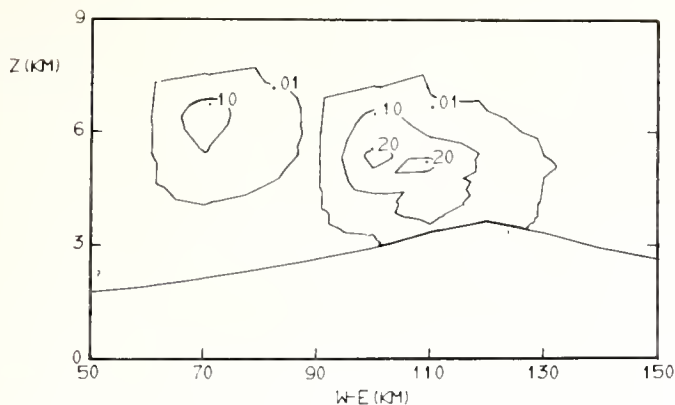


Figure 17. Mixing ratio of total ice (gm kgm^{-1}) along the wind at 2400 seconds into the integration.

although continuing distinct, now show signs in Figure 37 of merging. Total ice in excess of 0.30 gm kgm^{-1} is found at the 4-km level just upwind of the peaks. Figures 38, 39, and 40 show that unrimed crystals are now mainly falling on the peaks, and also are extending well over the leeward side. Partially rimed crystals and graupel are confined to the upwind slope, and their respective maxima have developed further upwind.

Cross-sections normal to the wind at 4500 seconds (Figs. 41–45) show cloud water has decreased in the saddle to about 0.20 gm kgm^{-1} . Maxima of total ice near 0.40 gm kgm^{-1} are located just above the peaks and to the saddle side of the summits. The upper portion of the orographic cloud is glaciated and composed solely of unrimed crystals. More unrimed ice is now settling on the higher peaks, whereas riming and graupel development is most pronounced in the saddle area.

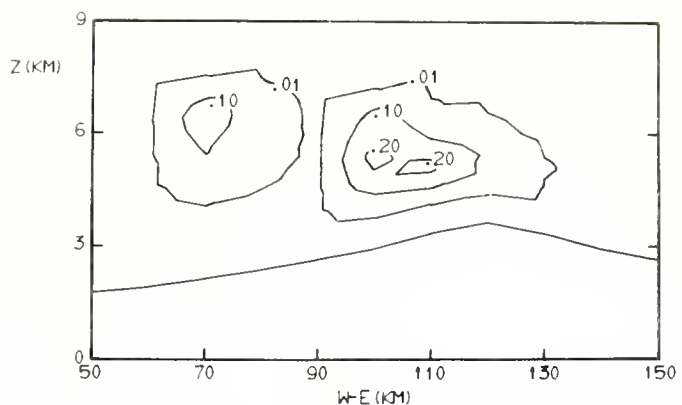


Figure 18. Mixing ratio of unrimed crystals (gm kgm^{-1}) along the wind at 2400 seconds into the integration.

Figures 46 and 47 show cloud water and total ice for a cross-section along the wind and through the middle of the saddle area. Note that the upwind edge of the 0.01 gm kgm^{-1} contours for cloud water and total ice are displaced 30 km to 40 km farther downwind than in a similar cross-section through the south peak. This reflects a different slope of the terrain along this cross-section.

Total snowfall during the 4500-second period is depicted in Figure 48. Note that the snowfall maxima are located upwind and to the saddle side of the peaks. Snowfall extends farther upwind along the higher flanks of the peaks than upwind of the lower saddle area. Measurable snowfall has also occurred to a point about 15 km leeward of the peaks. Snowfall maxima are slightly in excess of 0.20 cm of water equivalent, or about one inch of snow.

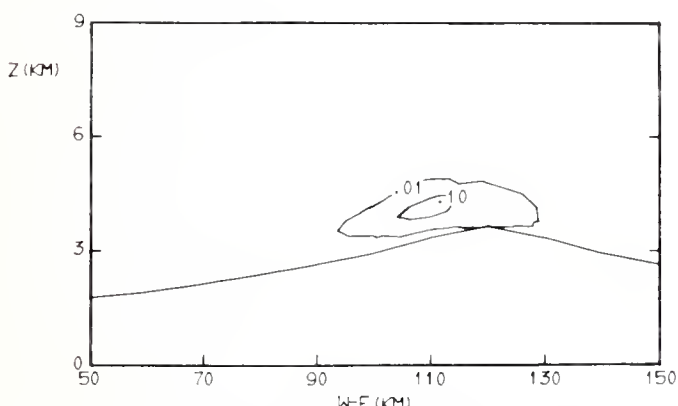


Figure 19. Mixing ratio of partially rimed crystals (gm kgm^{-1}) along the wind at 2400 seconds into the integration.

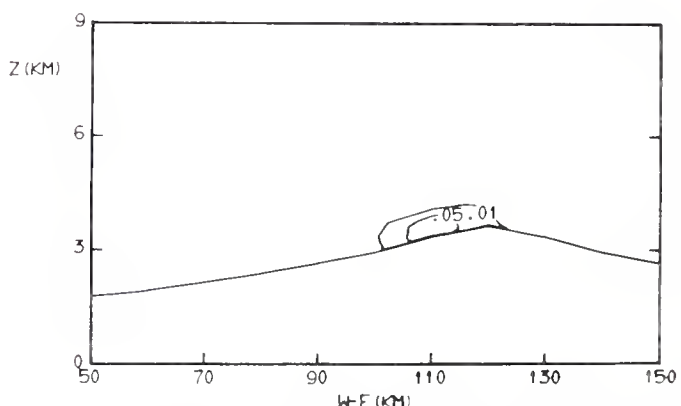


Figure 20. Mixing ratio of graupel (gm kgm^{-1}) along the wind at 2400 seconds into the integration.

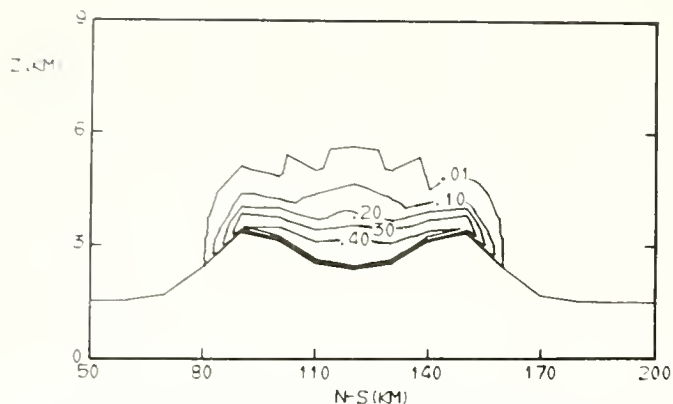


Figure 21. Mixing ratio of cloud water (gm kgm^{-1}) normal to the wind at 2400 seconds into the integration.

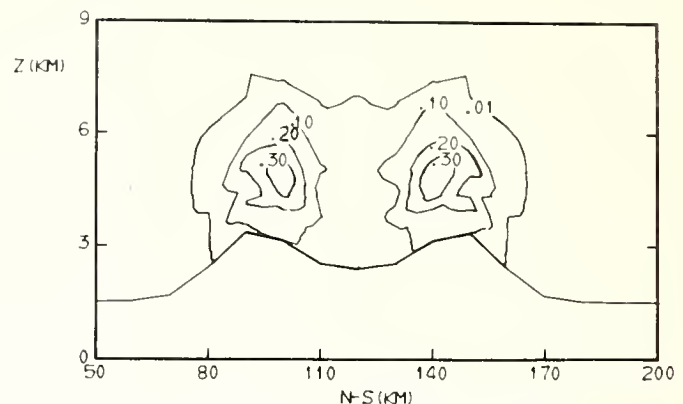


Figure 22. Mixing ratio of total ice (gm kgm^{-1}) normal to the wind at 2400 seconds into the integration.

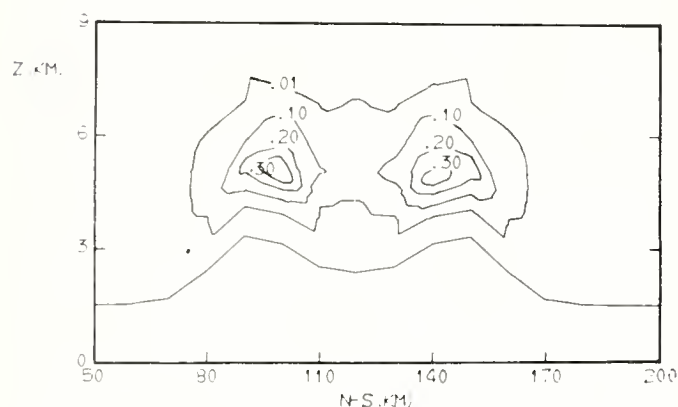


Figure 23. Mixing ratio of unrimed crystals (gm kgm^{-1}) normal to the wind at 2400 seconds into the integration.

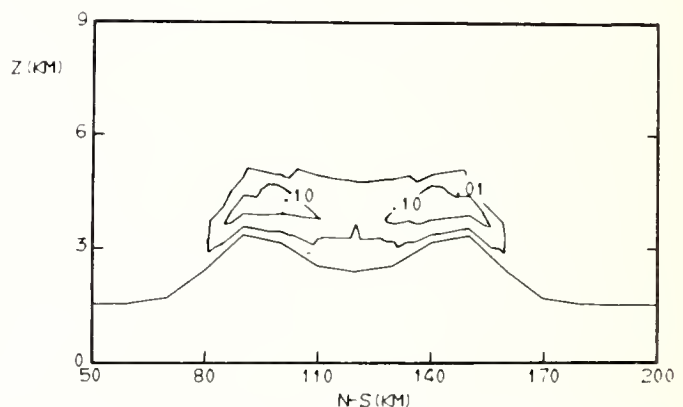


Figure 24. Mixing ratio of partially rimed crystals (gm kgm^{-1}) normal to the wind at 2400 seconds into the integration.

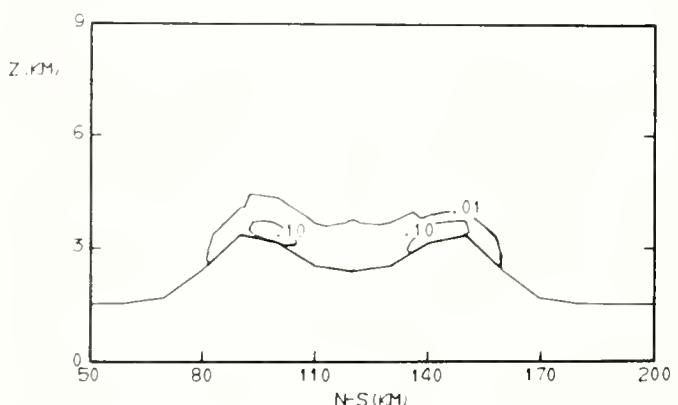


Figure 25. Mixing ratio of graupel (gm kgm^{-1}) normal to the wind at 2400 seconds into the integration.

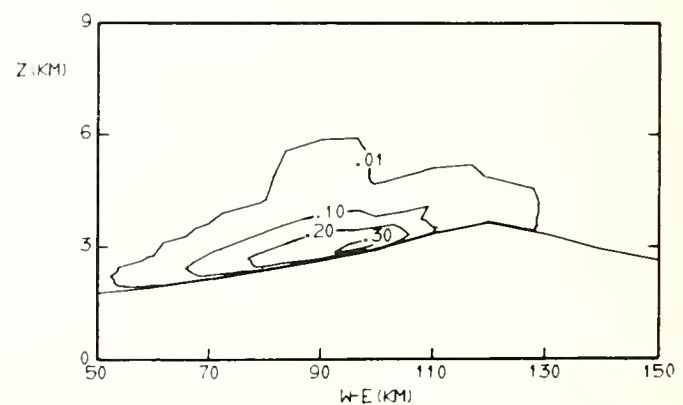


Figure 26. Mixing ratio of cloud water (gm kgm^{-1}) along the wind at 3750 seconds into the integration.

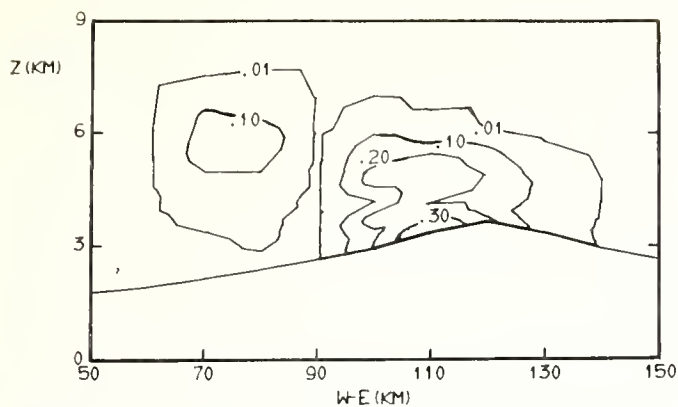


Figure 27. Mixing ratio of total ice (gm kgm^{-1}) along the wind at 3750 seconds into the integration.

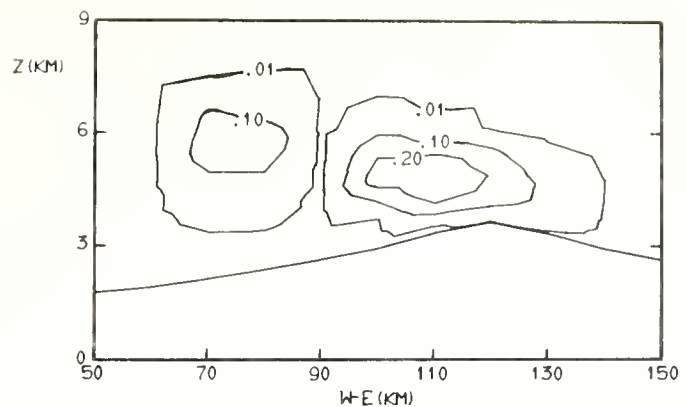


Figure 28. Mixing ratio of unrimed crystals (gm kgm^{-1}) along the wind at 3750 seconds into the integration.

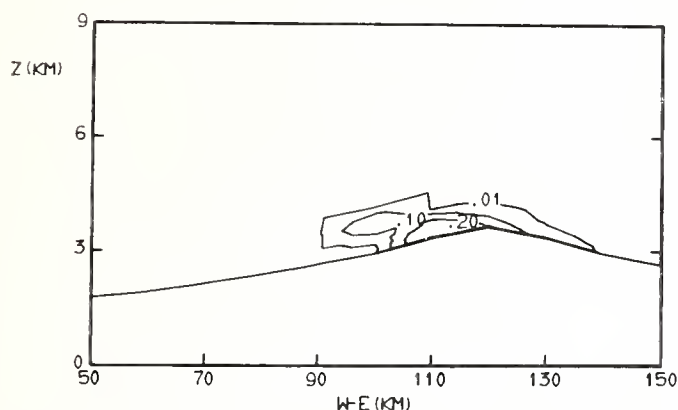


Figure 29. Mixing ratio of partially rimed crystals (gm kgm^{-1}) along the wind at 3750 seconds into the integration.

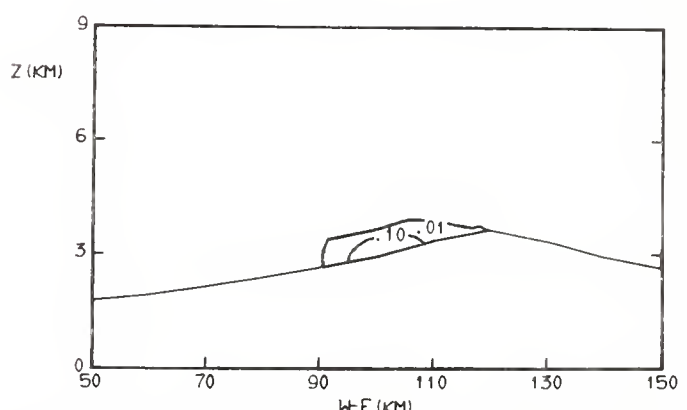


Figure 30. Mixing ratio of graupel (gm kgm^{-1}) along the wind at 3750 seconds into the integration.

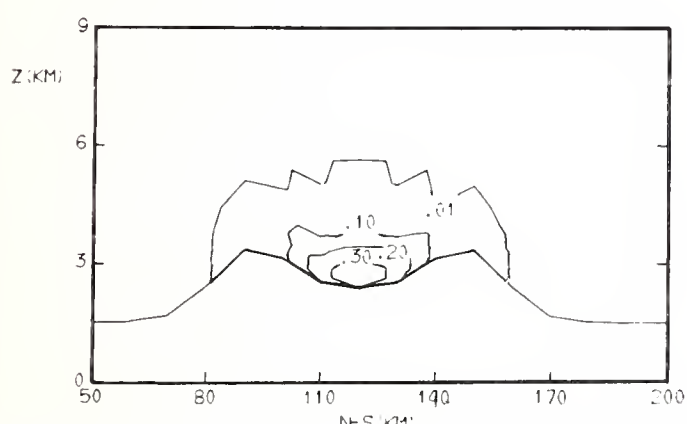


Figure 31. Mixing ratio of cloud water (gm kgm^{-1}) normal to the wind at 3750 seconds into the integration.

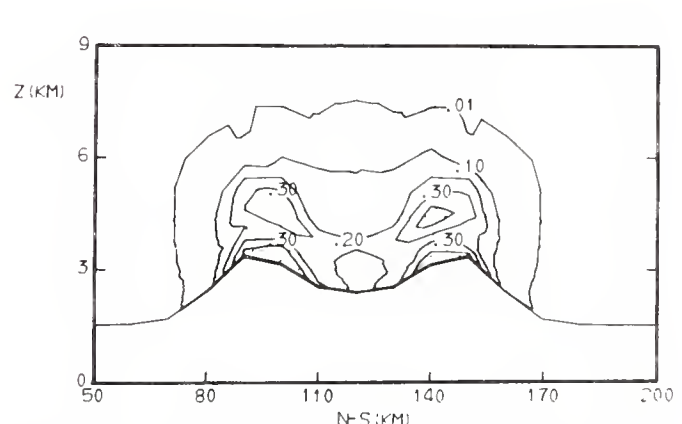


Figure 32. Mixing ratio of total ice (gm kgm^{-1}) normal to the wind at 3750 seconds into the integration. Dotted area denotes $q_i > 0.40 \text{ gm kgm}^{-1}$.

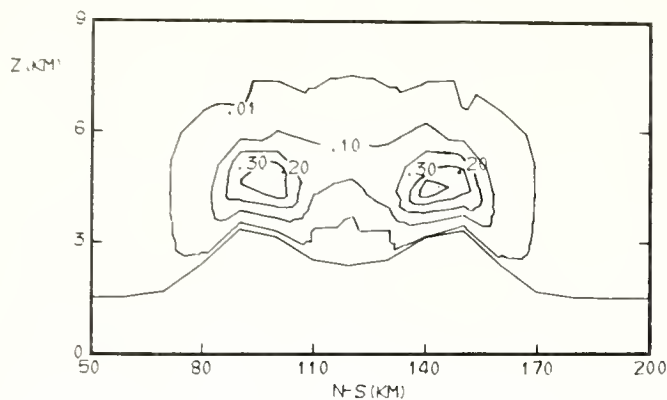


Figure 33. Mixing ratio of unrimed crystals (gm kgm^{-1}) normal to the wind at 3750 seconds into the integration.

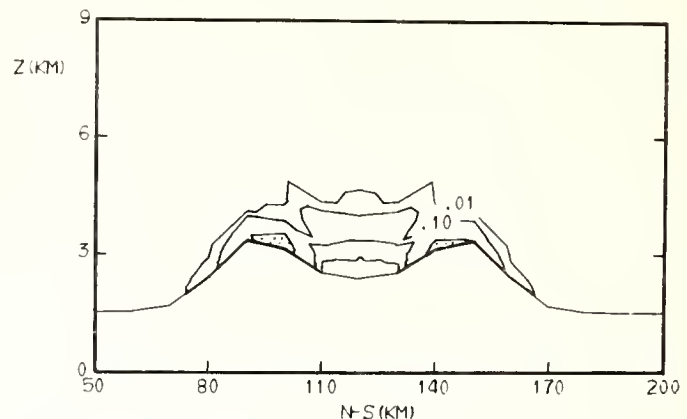


Figure 34. Mixing ratio of partially rimed crystals (gm kgm^{-1}) normal to the wind at 3750 seconds into the integration. Dotted area denotes $q_p > 0.20 \text{ gm kgm}^{-1}$.

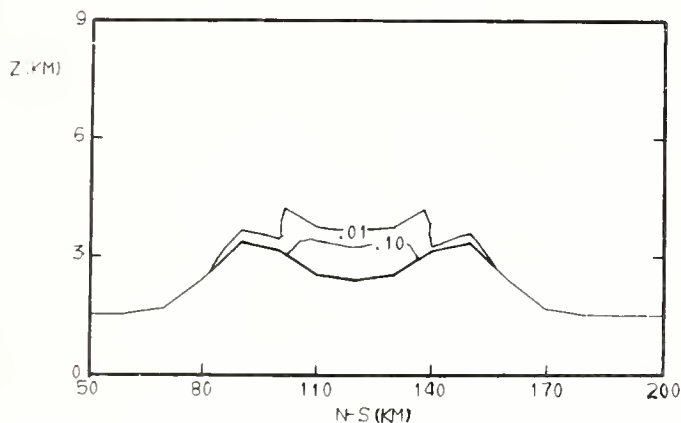


Figure 35. Mixing ratio of graupel (gm kgm^{-1}) normal to the wind at 3750 seconds into the integration.

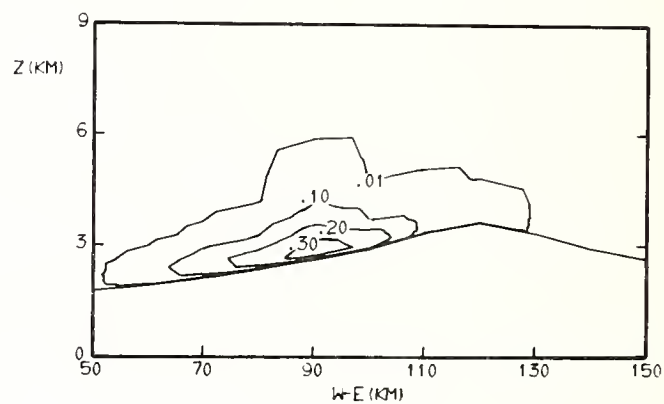


Figure 36. Mixing ratio of cloud water (gm kgm^{-1}) along the wind at 4500 seconds into the integration.

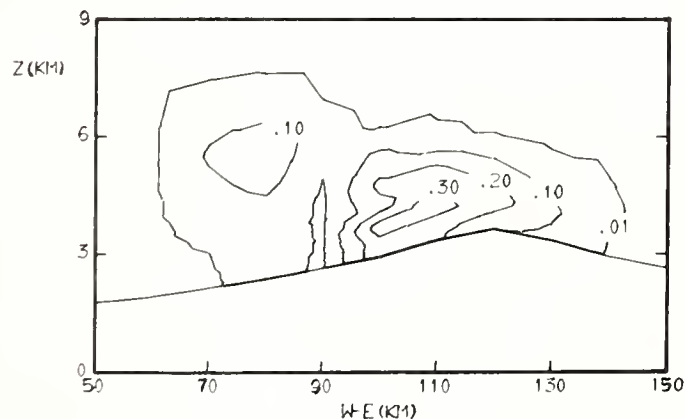


Figure 37. Mixing ratio of total ice (gm kgm^{-1}) along the wind at 4500 seconds into the integration.

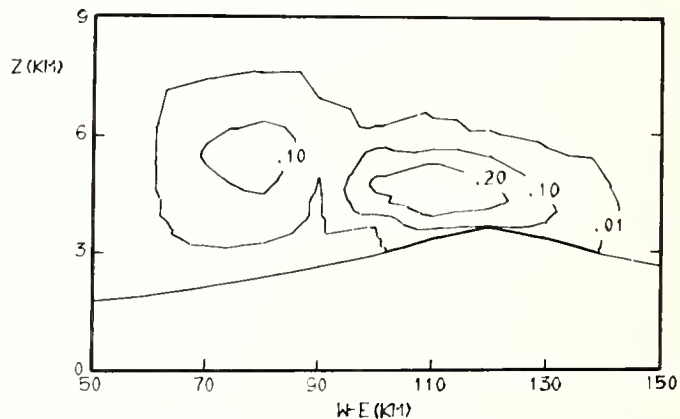


Figure 38. Mixing ratio of unrimed crystals (gm kgm^{-1}) along the wind at 4500 seconds into the integration.

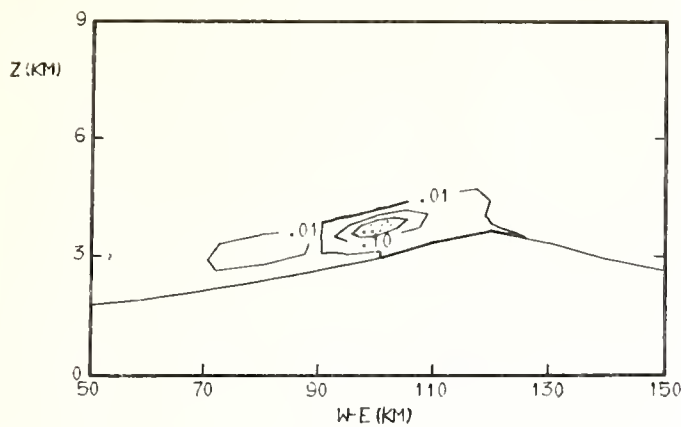


Figure 39. Mixing ratio of partially rimed crystals (gm kgm^{-1}) along the wind at 4500 seconds into the integration. Dotted area denotes $q_p > 0.20 \text{ gm kgm}^{-1}$.

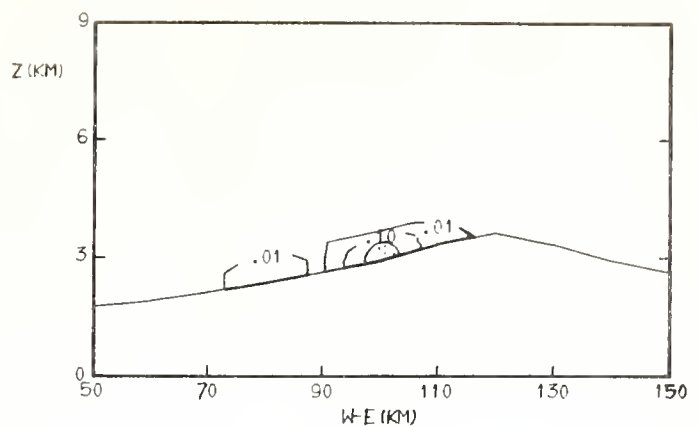


Figure 40. Mixing ratio of graupel (gm kgm^{-1}) along the wind at 4500 seconds into the integration. Dotted area denotes $q_p > 0.20 \text{ gm kgm}^{-1}$.

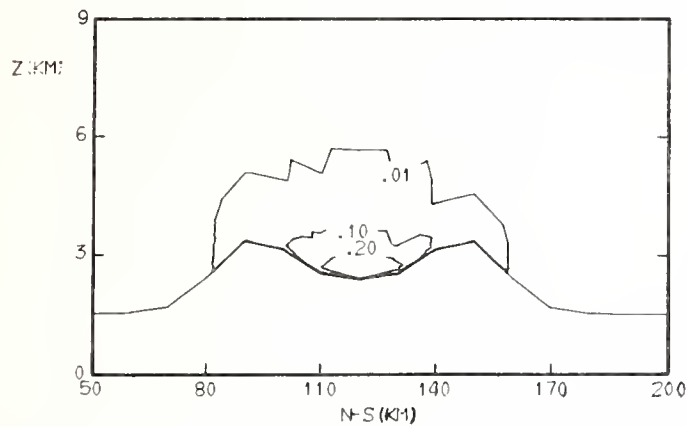


Figure 41. Mixing ratio of cloud water (gm kgm^{-1}) normal to the wind at 4500 seconds into the integration.

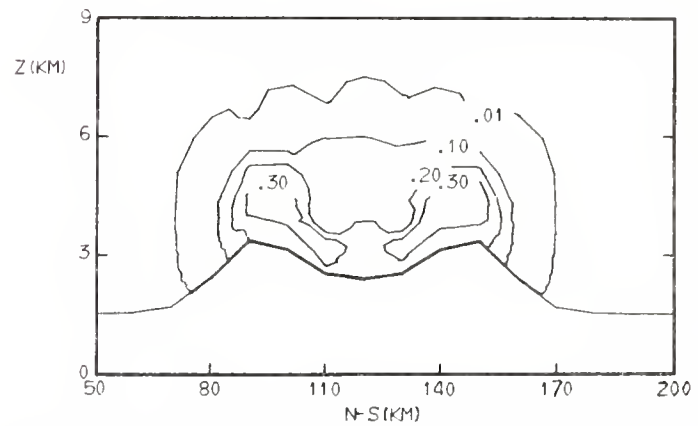


Figure 42. Mixing ratio of total ice (gm kgm^{-1}) normal to the wind at 4500 seconds into the integration.

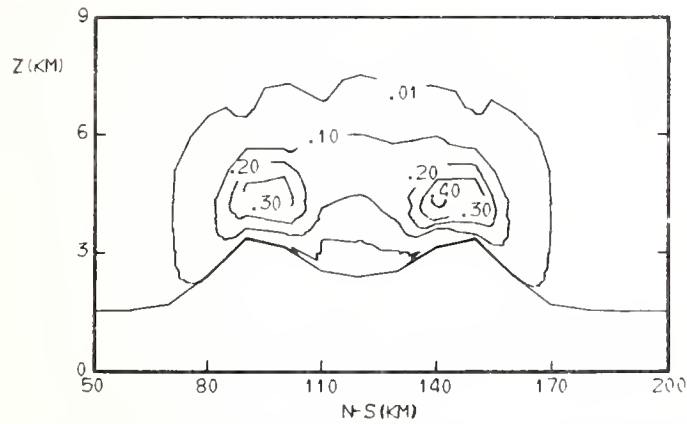


Figure 43. Mixing ratio of unrimed crystals (gm kgm^{-1}) normal to the wind at 4500 seconds into the integration.

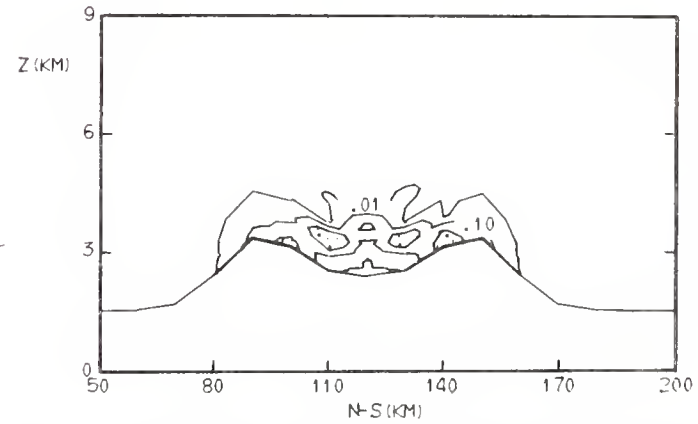


Figure 44. Mixing ratio of partially rimed crystals (gm kgm^{-1}) normal to the wind at 4500 seconds into the integration. Dotted area denotes $q_p > 0.20 \text{ gm kgm}^{-1}$.

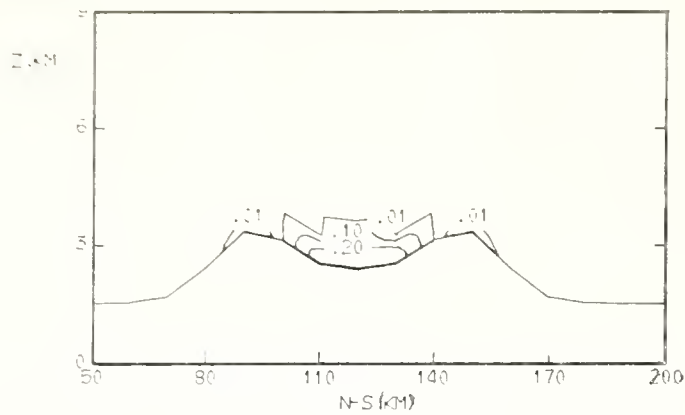


Figure 45. Mixing ratio of graupel (gm kgm^{-1}) normal to the wind at 4500 seconds into the integration.

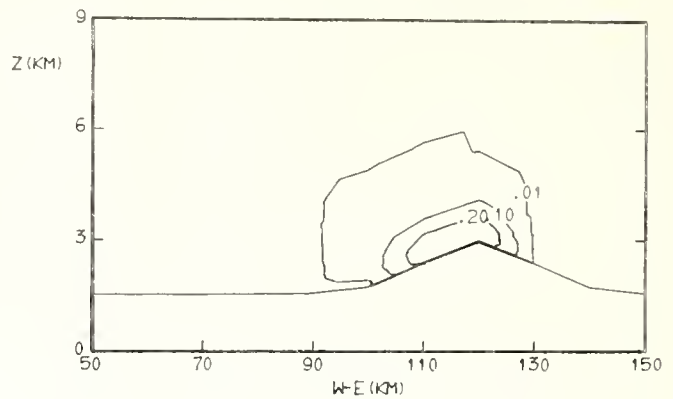


Figure 46. Mixing ratio of cloud water (gm kgm^{-1}) along the wind and through the saddle at 4500 seconds into the integration.

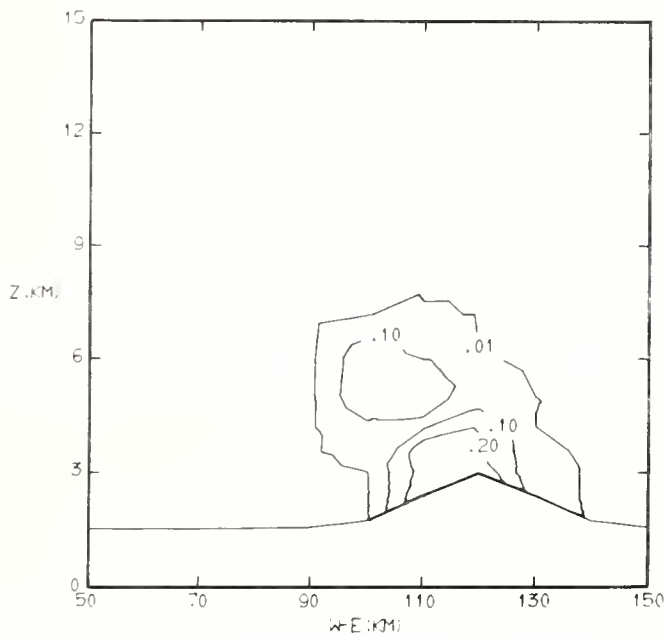


Figure 47. Mixing ratio of total ice (gm kgm^{-1}) along the wind and through the saddle at 4500 seconds into the integration.

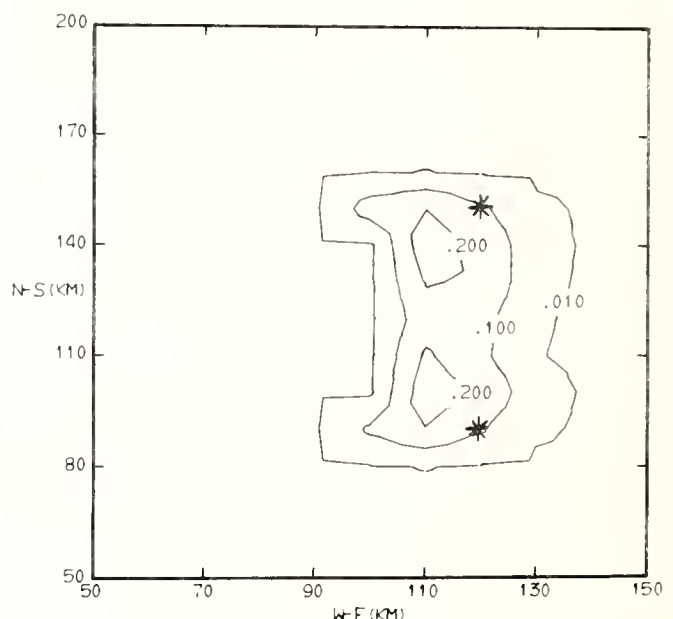


Figure 48. Snow depth ($\text{cm H}_2\text{O}$ equivalent) at 4500 seconds into the integration. Stars denote locations of mountain peaks.

6. SUMMARY AND DISCUSSION

A three-dimensional mesoscale model with cold cloud microphysics has been developed. The microphysical model partitions ice particles into three categories, each with its own set of physical characteristics. Growth by deposition and accretion of supercooled droplets is integrated over the particle populations in each category and summed to define the total ice growth. Besides deposition and accretion, other processes included in the model are condensation, evaporation, sublimation, sedimentation, and nucleation. Criteria for converting from one ice particle category to another are based on a comparison of accretional to depositional growth rates.

The model has been used to investigate the development and distribution of snowfall over a mountain massif. It appears to simulate realistically the nucleation and growth of ice particles, and their transport and sedimentation to the mountain surface. The leeward extent of snowfall (about 15 km) appears consistent with that frequently observed along the continental divide of Colorado for similar wind regimes.

Concentrations of ice particles were typically 3 to 10 liter⁻¹ during the run, which seems reasonable for the particular input sounding and ice nucleus activation spectrum used in the run. The maximum snow depth of approximately 0.2 cm H₂O equivalent for the 4500-second run also appears reasonable. This converts to approximately one inch of snowfall for the period.

Much development work remains. We plan to investigate the sensitivity of the model to the upper limit of integration specified for the Marshall-Palmer distributions. Further work is also needed to define the minimum concentration of particles necessary to constitute such a distribution. This is a problem when nucleation of ice crystals proceeds very slowly or when particle concentrations are sublimating away.

In preparation for verifying the model, we plan to introduce real terrain into the model and obtain stable flow solutions from the dynamical equations. Then, a first attempt will be made to compare the model with an actual precipitation episode over the Colorado Rockies. Observations of precipitation rates, crystal sizes, and riming should help "tune" the model by furnishing the data required to define collection efficiencies and the conversion criteria.

The presence of the mountain barrier leads to an adjustment in the initially uniform horizontal wind field, and the development of a vertical motion field within the model domain. This evolutionary process has important consequences when microphysical processes are included. The evolving vertical motion field can initiate condensation and start a sequence of microphysical events. Characteristics of this chain of events are therefore sensitive to the initial timing and location of condensation. It follows that future validation studies of precipitation using real data will require a careful examination of the initialization procedure.

Several areas of uncertainty remain with respect to the prediction and modification of snowfall over mountainous terrain. One is the effect of blocking on the air flow, and the transport of seeding materials toward and over the mountain barrier. Second, there is a need to better differentiate the net areal modification of snowfall from possible illusory results that arise from the redistribution of snowfall over the mountain barrier. Third, there are possible effects of natural seeding as ice crystals fall out from higher cloud layers, survive a trip through a cloudless layer, and resume growth as they enter a lower cloud system. Also, it is possible that ice crystals exiting an orographic barrier may survive to seed cloud layers further downwind. The mesoscale model presented here has the capability to investigate and explore these uncertainties. Furthermore, since microphysical processes are coupled back into the dynamical prediction equations, this model can define dynamic effects associated with various seeding treatments. Finally, various seeding strategies can be studied within the model to develop a design for bringing about beneficial results, including targeting of snowfall over mountainous regions.

7. ACKNOWLEDGMENTS

We thank E. L. Magaziner, E. C. Nickerson, and J. M. Fritsch for many helpful discussions during the model development. This work has been partially supported by the Division of Atmospheric Water Resources Management, Bureau of Reclamation, Dept. of the Interior, Contract 14-06-D 7676, for which we are grateful.

8. REFERENCES

- Arakawa, A., and Y. Mintz, 1974: The UCLA general circulation model. Notes distributed at the workshop, 25 March–4 April. Dept. of Meteorology, UCLA.
- Auer, A. H., Jr. and D. L. Veal, 1970: The dimension of ice crystals in natural clouds. *J. Atmos. Sci.*, **27**, 919-926.
- Brown, S. R., 1970: Terminal velocities of ice crystals. *Atmos. Sci. Paper 170*, Dept. of Atmos. Sci., Colorado State Univ., Ft. Collins, 52 pp.
- Chappell, C. F., 1970: Modification of cold orographic clouds. Ph.D. Thesis, Colorado State University, 196 pp.
- Chappell, C. F. and F. L. Johnson; 1974: Potential for snow augmentation in cold orographic clouds. *J. Appl. Meteorol.*, **13**, 374-382.
- Cotton, W. R., 1972: Numerical simulation of precipitation development in supercooled cumuli. Part II. *Mon. Weather Rev.*, **100**, 764-784.
- Deardorff, J. W., 1972: Parameterization of the planetary boundary layer for use in general circulation models. *Mon. Weather Rev.* **100**, 93-106.
- Hobbs, P. V., R. C. Easter, and A. B. Fraser, 1973: A theoretical study of the flow of air and the fallout of solid precipitation over mountainous terrain. Part II. Microphysics. *J. Atmos. Sci.*, **30**, 813-823.
- Giusto, J. E., 1967: Nucleation factors in the development of clouds. Ph.D. Dissertation, Pennsylvania State Univ., 124 pp.
- Giusto, J. E., 1971: Crystal development and glaciation of supercooled cloud. *J. Rech. Atmos.*, **5**, 2, 69-85.
- Lin, J. T., H. T. Liu, and Y. H. Pao, 1974: Laboratory simulation of plume dispersion in stably stratified flows over complex terrain, Flow Research Report No. 29, Flow Research, Inc., Kent, Washington.
- Nakaya, U. and T. Terada, 1934: Simultaneous observations of the mass, falling velocity, and form of individual snow crystals. *J. Fac. Sci., Hokkaido Univ., Ser. 2*, **1**, 191-201.
- Nickerson, E. C. and E. L. Magaziner, 1976. The numerical simulation of orographically induced non-precipitating clouds. NOAA Tech. Report, ERL 377-APCL 39.
- Plooster, M. N. and N. Fukuta, 1975: A numerical model of precipitation from seeded and unseeded cold orographic clouds. *J. Appl. Meteorol.*, **14**, 859-867.
- Vardiman, L. and C. L. Hartzell, 1973: An investigation of precipitating ice crystals from natural and seeded winter orographic clouds. Report SR-359-33 by Western Scientific Services, Inc. to the Bureau of Reclamation under Contract No. 14-06-D-6644, 122 pp.
- Young, K. C., 1974: A numerical simulation of wintertime orographic precipitation. Part I. Description of model microphysics and numerical techniques. *J. Atmos. Sci.*, **31**, 1735-1748.

Appendix

SYMBOLS

a	Parameter in the temperature activation spectrum for ice nuclei	F_g	Ventilation factor for graupel particles
A	Cross-sectional area of crystal	F_p	Ventilation factor for partially rimed crystals
c_u	Thickness of unrimed planar crystal	F_u	Ventilation factor for unrimed crystals
C_n	Production of crystals by nucleation	F_{gi}	Vertical flux of graupel ice relative to the updraft
C_{gd}	Production of graupel particles by flux divergence	F_{gp}	Vertical flux of graupel particles relative to the updraft
C_{qs}	Production of graupel particles by sedimentation	F_{pi}	Vertical flux of partially rimed ice relative to the updraft
C_{pd}	Production of partially rimed crystals by flux divergence	F_{pp}	Vertical flux of partially rimed crystals relative to the updraft
C_{ps}	Production of partially rimed crystals by sedimentation	F_{ui}	Vertical flux of unrimed ice relative to the updraft
C_{ud}	Production of unrimed crystals by flux divergence	F_{up}	Vertical flux of unrimed crystals relative to the updraft
C_{us}	Production of unrimed crystals by sedimentation	G	Thermodynamic function
D	Diffusivity of water vapor in air	K	Thermal conductivity of air
D_c	Crystal conversion diameter (unrimed to partially rimed)	L_s	Latent heat of sublimation
D_d	Crystal conversion diameter (partially rimed crystal)	m_g	Mass of a graupel particle
D_g	Diameter of graupel particle	m_n	Average mass of a new crystal after nucleation
D_p	Diameter of partially rimed crystal	m_p	Mass of a partially rimed crystal
D_u	Diameter of unrimed crystal	m_u	Mass of an unrimed crystal
D_{qs}	Diameter of maximum graupel particle that will sublime in a model time step	n_g	Number of small graupel particles in the distribution
D_{ps}	Diameter of maximum partially rimed crystal that will sublime in a model time step	n_p	Number of small partially rimed crystals in the distribution
D_{us}	Diameter of maximum unrimed crystal that will sublime in a model time step	n_u	Number of small unrimed crystals in the distribution
e_i	Saturation vapor pressure over a plane surface	N_e	Parameter in the temperature activation spectrum for ice nuclei
E	Collection efficiency of crystals for supercooled cloud droplets	N_n	Concentration of ice nuclei effective at a given supercooling
f_1	Ratio of accretional growth to depositional growth for unrimed crystals	N_g	Total concentration of particles in the graupel distribution
f_2	Ratio of accretional growth to depositional growth for partially rimed crystals	N_p	Total concentration of particles in the partially rimed crystal distribution

N_u	Total concentration of particles in the unrimed crystal distribution	q_u	Mixing ratio of unrimed ice in the distribution
N_{gs}	Concentration of graupel particles with diameters less than D_{gs}	q_{cw}	Mixing ratio of cloud water
N_{pg}	Concentration of partially rimed crystals converting to graupel particles	q_{pg}	Mixing ratio of partially rimed ice converting to graupel ice
N_{ps}	Concentration of partially rimed particles with diameters less than D_{ps}	q_{up}	Mixing ratio of unrimed ice converting to partially rimed ice
N_{up}	Concentration of unrimed crystals converting to partially rimed crystals	r_u	Radius of unrimed planar crystal
N_{us}	Concentration of unrimed particles with diameters less than D_{us}	R_e	Reynolds Number
p	Pressure	R_v	Specific gas constant for water vapor
P_n	Nucleation rate of unrimed ice	S_i	Supersaturation with respect to a plane ice surface
P_{gd}	Production of graupel ice by flux divergence	t	Time
P_{gg}	Production of graupel ice by growth processes	T	Temperature
P_{gp}	Production of partially rimed ice by growth processes	u	West component of the horizontal wind velocity
P_{gs}	Production of graupel ice by sedimentation	v	South component of the horizontal wind velocity
P_{gu}	Production of unrimed ice by growth processes	V_g	Fall speed of graupel particle
P_{pd}	Production of partially rimed ice by flux divergence	V_p	Fall speed of partially rimed crystal
P_{ps}	Production of partially rimed ice by sedimentation	V_u	Fall speed of unrimed crystal
P_{ud}	Production of unrimed ice by flux divergence	w	Vertical velocity
P_{us}	Production of unrimed ice by sedimentation	x, y	Horizontal coordinates
q_g	Mixing ratio of graupel ice in the distribution	z	Altitude and vertical coordinate
q_i	Mixing ratio of total ice	Δt	Model time step
q_p	Mixing ratio of partially rimed ice in the distribution	λ_g	Parameter in graupel particle distribution
		λ_p	Parameter in partially rimed crystal distribution
		λ_u	Parameter in unrimed crystal distribution
		ρ	Air density
		ν	Kinematic viscosity

Environmental Research LABORATORIES

The mission of the Environmental Research Laboratories (ERL) is to conduct an integrated program of fundamental research, related technology development, and services to improve understanding and prediction of the geophysical environment comprising the oceans and inland waters, the lower and upper atmosphere, the space environment, and the Earth. The following participate in the ERL missions:

MESA	<i>Marine EcoSystems Analysis Program.</i> Plans, directs, and coordinates the regional projects of NOAA and other federal agencies to assess the effect of ocean dumping, municipal and industrial waste discharge, deep ocean mining, and similar activities on marine ecosystems	GFDL	<i>Geophysical Fluid Dynamics Laboratory.</i> Studies the dynamics of geophysical fluid systems (the atmosphere, the hydrosphere, and the cryosphere) through theoretical analysis and numerical simulation using powerful, high-speed digital computers.
OCSEA	<i>Outer Continental Shelf Environmental Assessment Program.</i> Plans, directs, and coordinates research of federal, state, and private institutions to assess the primary environmental impact of developing petroleum and other energy resources along the outer continental shelf of the United States.	APCL	<i>Atmospheric Physics and Chemistry Laboratory.</i> Studies cloud and precipitation physics, chemical and particulate composition of the atmosphere, atmospheric electricity, and atmospheric heat transfer, with focus on developing methods of beneficial weather modification.
WM	<i>Weather Modification Program Office.</i> Plans, directs, and coordinates research within ERL relating to precipitation enhancement and mitigation of severe storms. Its National Hurricane and Experimental Meteorology Laboratory (NHEML) studies hurricane and tropical cumulus systems to experiment with methods for their beneficial modification and to develop techniques for better forecasting of tropical weather. The Research Facilities Center (RFC) maintains and operates aircraft and aircraft instrumentation for research programs of ERL and other government agencies.	NSSL	<i>National Severe Storms Laboratory.</i> Studies severe-storm circulation and dynamics, and develops techniques to detect and predict tornadoes, thunderstorms, and squall lines.
AOML	<i>Atlantic Oceanographic and Meteorological Laboratories.</i> Studies the physical, chemical, and geological characteristics and processes of the ocean waters, the sea floor, and the atmosphere above the ocean.	WPL	<i>Wave Propagation Laboratory.</i> Studies the propagation of sound waves and electromagnetic waves at millimeter, infrared, and optical frequencies to develop new methods for remote measuring of the geophysical environment.
PMEL	<i>Pacific Marine Environmental Laboratory.</i> Monitors and predicts the physical and biological effects of man's activities on Pacific Coast estuarine, coastal, deep-ocean, and near-shore marine environments.	ARL	<i>Air Resources Laboratories.</i> Studies the diffusion, transport, and dissipation of atmospheric pollutants; develops methods of predicting and controlling atmospheric pollution; monitors the global physical environment to detect climatic change.
GLERL	<i>Great Lakes Environmental Research Laboratory.</i> Studies hydrology, waves, currents, lake levels, biological and chemical processes, and lake-air interaction in the Great Lakes and their watersheds; forecasts lake ice conditions.	AL	<i>Aeronomy Laboratory.</i> Studies the physical and chemical processes of the stratosphere, ionosphere, and exosphere of the Earth and other planets, and their effect on high-altitude meteorological phenomena.
		SEL	<i>Space Environment Laboratory.</i> Studies solar-terrestrial physics (interplanetary, magnetospheric, and ionospheric); develops techniques for forecasting solar disturbances; provides real-time monitoring and forecasting of the space environment.

PENN STATE UNIVERSITY LIBRARIES



A000072021804